

Increasing the bit density of a quantum confinement physically unclonable function.

By

Hamzah Shokeir



Lancaster University

Department of Physics

Lancaster University

September 2017

A dissertation submitted in partial fulfilment of the requirements for the degree Masters of Science
(By Research)

Declaration

This thesis is the result of work carried out at Lancaster University between October 2016 and September 2017 and in collaboration with IMDEA Nanociencia. I declare that the work presented was carried out solely and contains nothing which is the result of work done in association with others, except as specified in the text and references. The thesis is not substantially the same as any I have already submitted, or that I am in the process of submitting, for any degree at any university. This thesis does not exceed 30,000 words.

H.Shokeir,

A handwritten signature in black ink, appearing to read 'H. Shokeir', with a horizontal line extending from the end of the signature.

Lancaster,

2017.

“Beautiful is what we see, more beautiful is what we know.

Most beautiful is by far, what we don’t”

-Nicolos Steno

1638-1686.

Acknowledgements

I would like to start by thanking my supervisor Prof. Robert Young who has given me the rare opportunity to embark on scientific research. His generosity, expertise and work ethic is an example for me to follow throughout my scientific career. This has been by far the most valuable year in my scientific and academic life and I am forever grateful for such.

I extend my thanks to our collaborators at IMDEA Nanociencia; Daniel Granados Ruíz and Manuel Rodríguez Osorio who made this project possible, I am forever indebted for their time and effort and for facilitating a huge part of this research.

Much of the achievements and attainments would not have been possible without the help and support of Ramon Benardo-Gavito who has been a great mentor this year and a source of inspiration at times. And Thomas McGrath who put up with my dim moments and was one of the kindest individuals to work with. You are both great scientists thank you to both of you, not all heroes wear capes!

Thank you Chris Woodhead for assisting me in the helium flow cryostat setup, thank you Yassir Noori for assisting me in the SEM imaging and saving my hide in the last minute. Thank you Yameng Cao for useful discussions in understanding conceptual elements of the project. Thank you Ben for helping me out with the code. Thank you Johnny Roberts for getting me started into the project.

This would not have been possible without my family and loved ones. Thank you to my father for all his support, my mother for all her reassurance and my sister for reminding me why we scientists do what we do; to make the world a better place for our children; thank you for helping me achieve my dreams. And thank you to my darling Paulina, who made me see the light at the end of every tunnel. I love you all.

Summary

This dissertation presents work carried out in collaboration with the IMDEA nanoscience institute. We study the recently proposed quantum confinement physically unclonable function by Roberts, et al. that utilises resonant tunnelling diodes (physical representation of a quantum well) and atomic scale imperfections for applications in cryptography and identification. Presently such entities rely on their resonance peak position as the basis for a new approach to electronic identification systems.

By solely relying on the resonance peak of these devices deconvolution outputs an average of 8 bits per device, concatenation of up to 16 devices outputs a satisfactory number of bits for applications in uniqueness. However we explore the possibility of increasing the bit density of such physically unclonable functions that range from tangibly modifying the heterostructure with the use of a focused ion beam to induce quantum effects of 1 dimension (quantum wire) and 0 dimension (quantum dot) that would manifest its self as multiple resonance peaks observed on the current/voltage characteristic.

Our findings show multiple devices with consistent new features as a result of modification with the focused ion beam ultimately increasing the bit density. We carry out cryogenic measurements and comment on the fact that such features are not supported by previous work studying resonant tunnelling in the 1 & 0 states of double barrier heterostructures.

Table of Contents

Declaration.....	2
Acknowledgements.....	4
Summary.....	5
Chapter 1- The need for unique identities and increased bit density.....	8
1.1 Introduction.....	8
1.2 utilising physical disorder.....	8
1.3 Digitisation of RTD.....	11
1.4 Advancements and prospect.....	12
1.4 Current work and contributions.....	13
Bibliography.....	15
Chapter 2- The Physics of Semiconductors and the QCPUF.....	16
2.1 Introduction.....	16
2.2 Band structure, doping and III-V semiconductors.....	16
2.3 Doping and Fermi level pinning.....	17
2.4 Density of states: quantum wells, wires and dots.....	18
2.5 The Resonant Tunneling Diode.....	20
2.6 Fabrication of RTD.....	22
2.7 The PUF, QCPUF and RTD.....	22
2.8 The case of the strong PUF vs the weak PUF.....	23
2.9 Resonant tunneling through higher order sates.....	24
2.10 Temperature dependence of bandgap.....	26
Bibliography.....	28
Chapter 3- Experimental methods.....	29
3.1 Introduction.....	29
3.2 Scanning electron microscopy.....	29
3.3 Focused Ion Beam.....	30
3.4 Electronic characterisation.....	31
3.4.1 Source measure unit.....	32
3.4.2 Room temperature probe station.....	32
3.5 Micro Wire bonder.....	33
3.6 Low temperature measurements.....	35
3.6.1 Low temperature probe station.....	36
3.6.2 Helium flow cryostat.....	36
Bibliography.....	38
Chapter 4- Experimental Results.....	39

4.1 Introduction.....	39
4.2 Increased Bit Density	39
4.2.1-Introduction.....	39
4.2.2-Etch designs and parameters.	40
4.2.3-Lateral etch.....	41
4.2.4-Diamond etch.	43
4.2.4-Arrow etch.....	45
4.2.5-Ring+Rectangle etch.	45
4.2.6-Ring+Triangle Etch.	47
4.2.7-Hole Etch.	49
4.2.8-Square etch.....	51
4.2.9-Dot etch.....	52
4.3-Analysis	54
4.3.1 Defective devices	54
4.3.2 Increased Bit rate	55
4.3.4 Minute features superimposed in NDR.....	56
G1-Square etch.....	56
F10-Square Etch.....	57
B4-Lateral Etch	58
4.3.5 Low Temperature Measurements of Bumps.....	60
4.3.6 Discussion and Conclusion.....	63
Bibliography	65
Chapter 6 - Conclusions and Further Work.....	66
6.1 Conclusions.....	66
6.2 Further Work	67
Bibliography	69

Chapter 1- The Need for Unique Identities and Increased Bit Density.

1.1 Introduction

When Francis Galton first developed his theory of fingerprints and physiognomy, few would have anticipated the impact in the modern world. It has been noted that Galton's work contributed to the paradigm of absolute identification and that the biometric system is the absolute political weapon of the current era [1]. Today the use of fingerprints and biometrics is a corner stone of secure identification and security, the shift of our technologies advancing as well. Amidst the advancement of communication, financial transactions and the Internet of Things (IoT) the critical question of security lies behind every action. As we see the growth of such technologies in the coming years the cause for concern on the issue of trust is ever more great. Although we are now entering an era where advanced methods of cryptography are gaining much attention and spotlight in research (such as quantum cryptography). Counterfeit drugs contribute to a multi-billion dollar global business; according to a World Health Organisation study 450,000 people alone die annually in Africa as a result of fake malaria treatment [2]. It is not only a matter of technological importance but also of social, political and economic that our identification systems and methods guarantees a future without fakes.

Conventional systems of identification typically require the use of a key as the central entity for identification, such a key is usually stored digitally. The mere storage of a digital key in electronic hardware renders its self to attacks in cloning and learning [3]. What is required is a system that renders its self near impossible in cloning and attacking, it has been previously proposed that an entity that comprises of an inspirable link between its identity and physical structure would be an ideal candidate for assured identification [4].

1.2 Utilising physical disorder

Unique objects (UOs) and physically unclonable functions (PUF) consist of physical structures that are near impossible to replicate even given the exact manufacturing process. Their uses are versatile and can be applicable to identification, authentication and cryptography. Their uniqueness isn't necessary stored in alphanumeric format (i.e. digital memory) but rather are extracted from the physical structure they are. There exist a plethora of PUFs relying on different mechanisms such as the scattering pattern induced by an optical medium [5] or by relying on the variations of transistor switch delays [6]. Although such methods yield secure unclonable results they typically require an apparatus that limits their implementation in a practical setting such as everyday consumer use and in other cases where PUFs have been less successful, neural networks and other such machine learning techniques have 'cracked' and attacked such [6]. Although recently we have seen a surge in smaller scale PUFs such as with the use of carbon nanotubes [7] and in random access memory such are still not sensitive to the minutest of defects.

The notion that we can utilise the physical atomic disorder in quantum nanostructures and other such structures such as 2D materials was first introduced by Roberts et al. [4] and Cao et al. [8] respectively. Optical tags analogous to that of a barcode found on a banknote can be comprised from 2D materials and their minute defects, such imperfections and defects can be introduced during the fabrication stage of crystal growth which can simply be spatial variations in the bandgap or the comparison of different monolayer and thicker layer regions of the tag [8]. In Cao's work they were able to successfully characterise such imperfections from a transition metal dichalcogenide (TMDC), tungsten disulphide (WS_2) via photoluminescence (PL) measurements and with the use of simple optics. Further tests with atomic force microscopy verified their measurements that the uniqueness was indeed a result of the nanoscale variations. The advantage of manufacturing atom thick optical tags that can be used as UOs is that they can be readily imbedded on the surface of products such as bank note or a pharmaceutical. Cao's method provides a simple way to extract information based on the band pass filter orientation θ , bandwidth $\Delta\omega$ and the spatial variations from the PL measurements $PL(x,y)$.

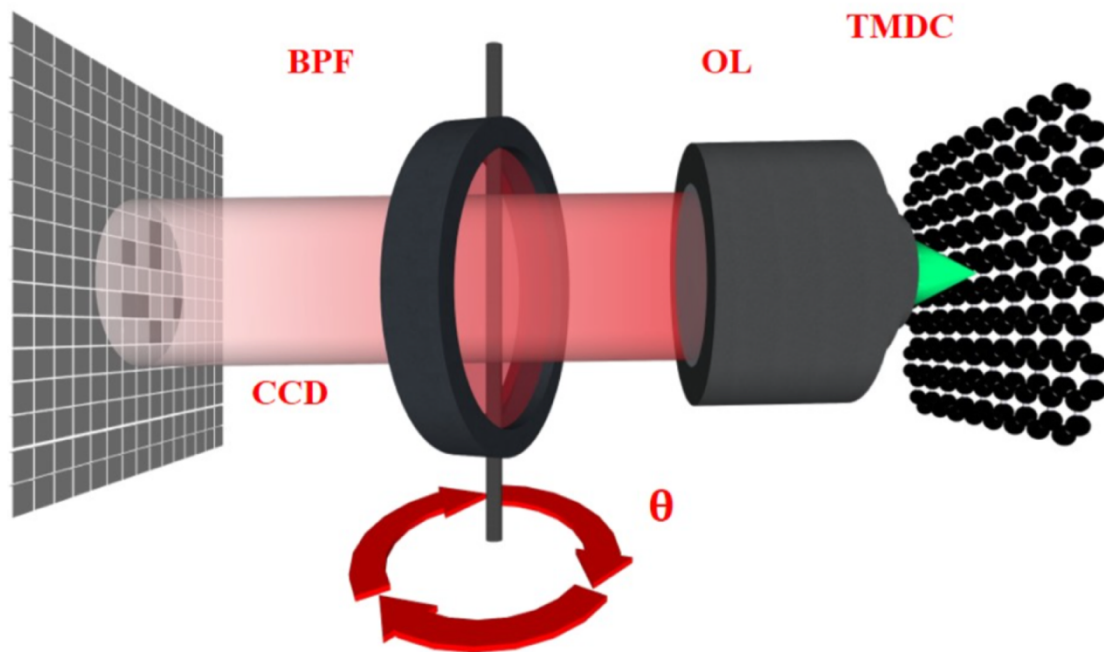


Figure 1.1a: Schematic displaying the protocol to extract information from TMDC, in this case: WS_2 . OL is the objective lens, θ is the angle of rotation of the bandpass filter (BPF) and the charge couple device (CCD) camera. [8]

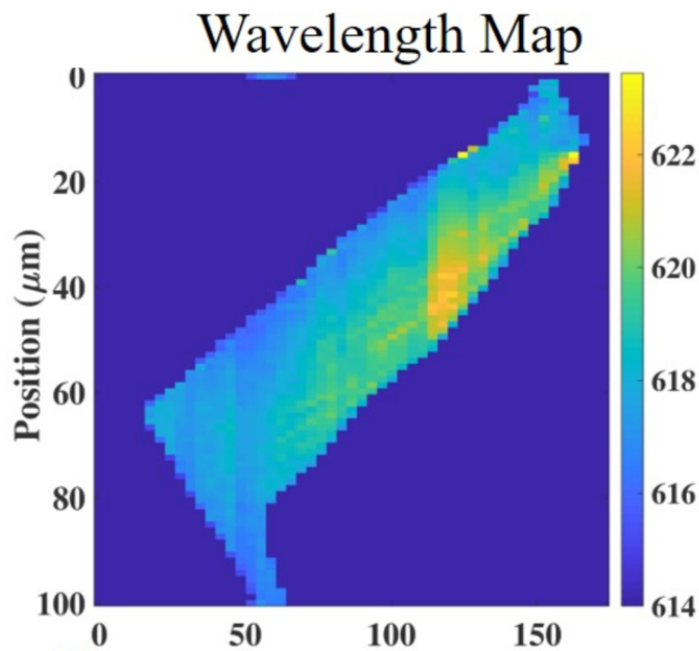


Figure 1.1b: A flake of WS₂ showing a PL map of peak wavelength [8].

On the other hand, we are able to rely not only on the variations measured by optical characteristics such as those stated above, but also on electrical characteristics based on the same notion that imperfections on the atomic scale induce changes that we are able to visualise and measure to a high precision. It has also been shown that in Roberts' work [4] that there exists an alternative to small scale optical practical PUF that can be implemented in everyday consumer life. However rather than relying on TMDC monolayer structures, Roberts' work showed that it is possible to utilise certain types of quantum heterostructures that follow the same formula for a secure PUF; namely relatively easy to fabricate yet infeasible to clone.

A quantum heterostructure is defined as a structure typically comprised of multiple layers of semiconducting materials that are arranged in such a way that charge carriers are confined in a select number of dimensions. Confining electrons otherwise known as quantum confinement induces quantum effects within the system, namely that discrete energy levels are formed. However, the exact positions of these energy levels are subject to a number of uncontrollable parameters that are in effect during the fabrication stage of these heterostructures. It has been proposed that resonant tunneling diodes (RTDs) as a proof of concept of such a PUF [4]. What makes the RTD a favourable candidate in realising a secure PUF is that just as before where atomic disorder induced minute yet detectable variations in bandgap the same also applies when fabricating such quantum heterostructures. The barriers associated with the RTD are a few atoms thick, this in turn causes minute atomic changes to contribute greatly to quantum confinement and tunneling.

Other factors also include: resonance state position, interfacial roughness etc. The RTD is a device that confines electrons in one dimension and can have a surface area as small as 4 μm² (Fig 1.2) and are able to operate with a power as low as 12 mW and outputs a characteristic current voltage (IV) characteristic [9], this makes them a favourable candidate in integrating such in circuits or alongside a microprocessor in a handheld device.

The mechanisms in which we extract the uniqueness from the RTD is arguably simpler than the aforementioned optical PUF, additionally the method of fabrication allows up to hundreds [9] of different PUFs to be fabricated at once.

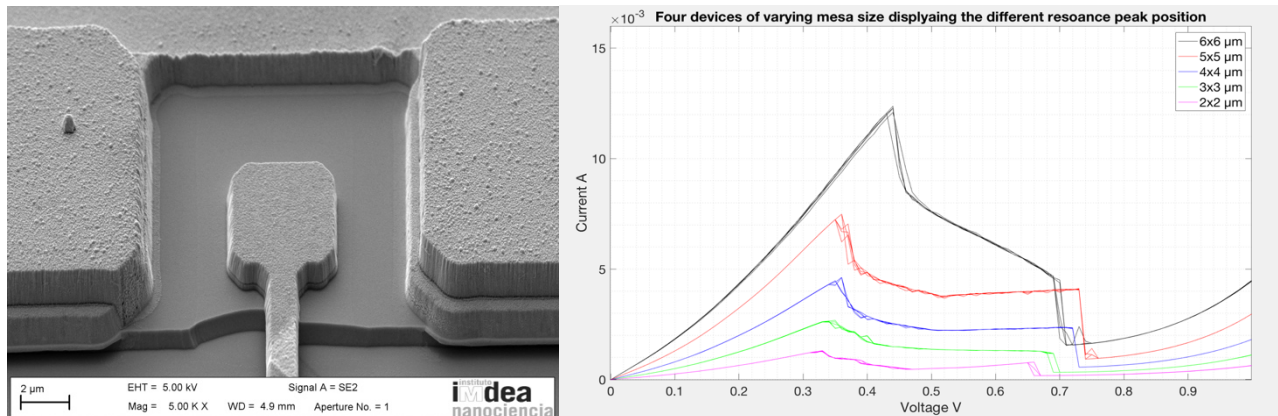


Figure 1.2: (Left) SEM image of RTD 4x4 μm sized mesa. (Right) four RTD of varying mesa size displaying their IV characteristic.

To measure such, we simply require a voltage source and a way of measuring output current. Such a setup can take the form of a standard source measure unit (SMU).

However despite its many advantages over the optical PUF, a major disadvantage is that we currently only rely on one aspect of each device to extract its uniqueness, namely that each PUF only has one component of uniqueness. Regardless, each device acts as an entirely unique object and hence can be implemented as a quantum confinement PUF (QCPUF).

1.3 Digitisation of RTD.

The central entity of our UO is the resonance position which exists as a peak in the device's IV characteristic. Various methods have been employed to test the uniqueness of these devices; one such [10] concatenates a number of devices in an attempt to increase the number of bits and compares the Hamming distance between the strings of bits extracted. The Hamming distance is defined as the difference between two strings of bits of equal length. A uniform distribution between two sets of concatenated devices would yield an average distance of 50%. Fig 1.3 c) shows that the average hamming distance of devices of 8 and 16 bits are 45.44% and 46.08% respectively. It has been previously proven [10] that a simple peak finding algorithm that utilises a Gaussian fit to find the peak position, our method of deconvolution into bits of data requires that we split our axis into bins (k) where the relationship between the number of bits (b) and bins scales logarithmically such that $b = \log_2(k)$. Figure 1.3a demonstrates such a scheme when $k=8$ bins gives us $b=3$ bits of data per device. It has been noted that three bits alone are insufficient in applications of cryptography or identification an increase in the number of bins would in turn cause an increase in the number of bits. However it is important to note that this scheme is limited in that we cannot arbitrarily increase the number of bins as this may compromise the robustness of the output.

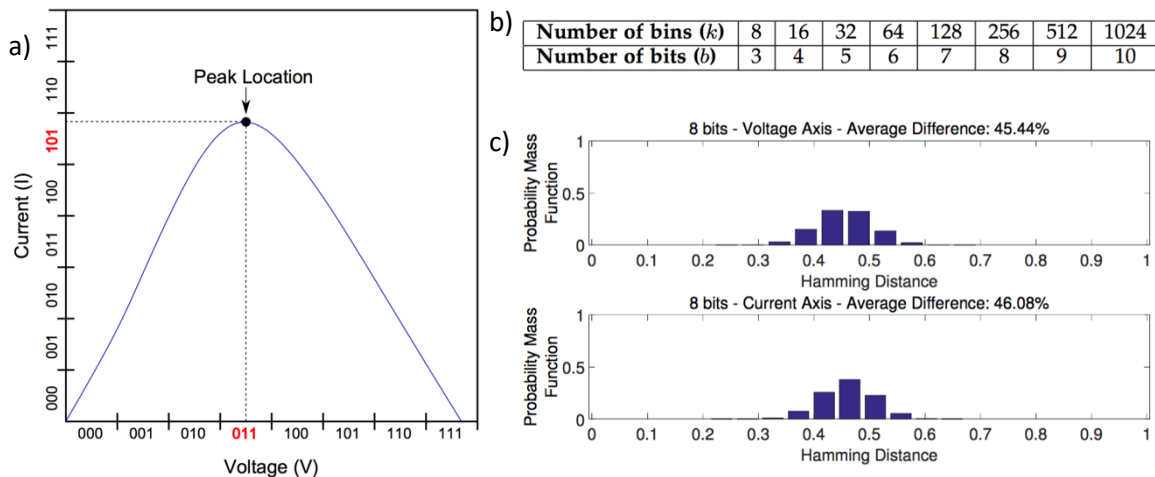


Figure 1.3: a) Gaussian distribution showing the peak location in terms of bits(101, 011) given the axis are divided into 8 bins. b) Table showing the evolution of bins (k) with bits (b). c) Hamming distance of strings of bits from concatenated devices of current and voltage (22 devices, 256 bins), from [10].

The result of concatenation would increase the total number of bits to B, the number of devices required to output a total number of bits B, where each device contributes b bits is give by $\varphi = B/b$. A sufficient number of bits ideally would be in the range of B=128. To achieve such one would require connecting multiple devices to extract multiple peaks, depending on the number of bins we assign per axis this would range from 16 to 22 devices. The tunneling region could also be used as a source of uniqueness as in principle is based on the same assumption that justifies our usage for the peak position. One could apply a linear regression that approximates a scalar term from the positive differential resistance then convert the scalar term to a binary sequence. However further investigation is required.

Given the advent of modern technology growing smaller and smaller the issue of scalability is not necessarily an immediate issue given the typical dimension of such devices however to realise a fingerprint like architecture of multiple minutia per sample we raise the problem: how are we able to extract more bits from a single device. Hence reducing the required number of RTDs to extract the ideal number of bits,

1.4 Advancements and prospect

Current fingerprint identification systems have advanced immensely since they were first implemented in forensics and other such fields. However, since their discovery and realisation in identification in the 1800s, the central concept on how we are able to extract uniqueness has remained the same throughout. During the verification phase a system scans the fingerprint for specific topographies known as minutiae. Such minutiae range from bifurcation to short ridges that randomly assorted on one's finger. Our methods of detecting such minutia have become increasingly more and more advanced as magnifying lenses have been replaced with CMOS image sensors. Although there exist multiple standards for minutiae recognition and identification [11], a standard approach requires a system that measure the distances and the angles between the minutiae and uses an algorithm that converts such data into a numeric code or a string of bits (Fig 1.4).

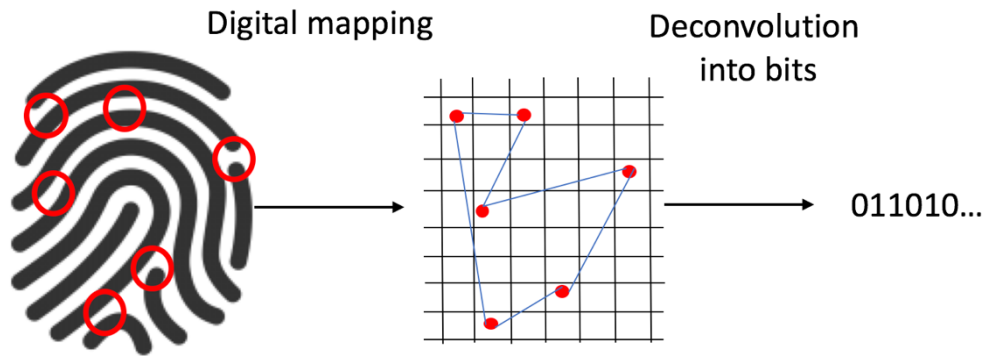


Figure 1.4: Schematic of how information is extracted from minutiae of fingerprint, mapped and digitised producing a string of binary data.

Generally the more fingers used, the greater the accuracy in identifying an individual and the greater number of minutiae used the greater the bit density of the extracted numeric code. Referring back to our analogy of using the IV peak position as a unique object similar to that of a fingerprint the question arises on how we can create further minutiae to maximise the complexity and hence increase the bit density of our QCPUF.

The central mechanism of the QCPUF is one dimensional quantum tunneling which relies on the presence of a quantum well heterostructure. We propose altering the structure in such a way that we create a greater dimensionality of confinement and hence have multiple resonance states that can be seen on the IV characteristic as multiple peaks. In order to create multiple confined regions, we must reduce the active area of the device significantly such that there is the presence of a quantum wire (2D) or quantum dot (3D).

1.5 Current work and contributions

Such raises the question of how one would embark on creating a structure with multiple confined states. Reengineering such structures from the fabrication stage is viable however we explore the possibility of modifying the structure post fabrication. We resort to the use of an etching process that allows us maximum control of not only the parameters but how we manipulate our etchant. We employed a focused ion beam (FIB) that allows us to alter the physical structure of our devices and aimed at introducing increased dimensions of confinement.

We explored up to 8 different etch designs with the FIB across over 69 devices. Our initial conclusions were such that designs that employed simple geometries that at the same time maximised the possibility of a confined active region produced the most interesting results. In essence, etching a square cavity (or similar) centred on the RTD mesa left constricted corners and lateral regions on the device. With said designs we observed consistent results that bare close resemblance to the results published by Tarucha Et al. [12].

Such consistent results were characterised as: 1) second resonance peak and 2) bumps within the NDR region. Prior to modifying our devices with the FIB, we recorded the IV characteristic in the negative bias (axis inverted), however at times we observed interesting features in both biases, as a comparison metric we were only able to compare our before and after sweeps in the negative bias. In many cases

we present only the IV characteristic under the negative bias, as generally broader peaks and larger PVR are observed under such bias. We also produced a set of devices whose final surface area was less than $4 \mu\text{m}^2$ (the current minimum of such RTDs) with a clear NDR region resulting in an increase in bit density per unit volume.

We begin the study by presenting the different designs for each etch type, in many cases the designs yielded non-functioning devices. Only a select few of the etch designs produced devices that were functioning post FIB and even fewer devices gave interesting results on the IV characteristic that were worth investigating.

We have stated the need for a new approach in how we identify our everyday objects, given the losses counterfeit products yield, methods that utilise intrinsic subatomic unpredictability have been proposed as an advanced means of security. Our proposition is to further utilise such features in a QCPUF and to create a fingerprint like architecture by introducing further minutiae.

In this chapter we have highlighted the need for secure identification and touched upon various novel approaches to using imperfections in nanostructures as a means of identification based on previous research. In chapter 2 we elaborate on the physics of semiconductor heterostructures and how our system can be utilised in unique identification. Chapter 3 reviews the experimental methods employed to study and modify our heterostructures, chapter 4 focuses on our results and analysis of our data. We conclude and suggest further work in chapter 5.

Bibliography

- [1] N. Lebovic, "Biometrics or the Power of the Radical Center", *Critical Inquiry*, 2015.
- [2] K.Kaliyaperumal, "The Counterfeit Anti-Malarial Is a Crime against Humanity: A Systematic Review of the Scientific Evidence," *Malaria Journal*, vol. 13, 2014.
- [3] A. B. L. K. I. & N. D. Barengi, "Fault injection attacks on cryptographic devices: theory, practise and countermeasures," in *Proc. IEEE*, vol. 100, p. 3056–3076, 2012.
- [4] J. Roberts, "Using Quantum Con nement to Uniquely Identify Devices," *Scientific Reports*, 2015.
- [5] R. B. T. J. a. G. N. Pappu R, "Physical one-way functions," *Science*, vol. 297, no. 5589, pp. 2026-2030, 2002.
- [6] S. F. S. J. D. G. D. S. a. S. J. Rü'hrmair U, "Modeling attacks on physical unclonable functions," "*Proceedings of the 17th ACM Conference on Computer and Communications Security CCS*", p. 237–249, 2010.
- [7] H. L. K. C. D. a. W. M. D. F. Konigsmark S T C, "Cnpuf: "A carbon nanotube-based physically unclonable function for secure low-energy hardware design," *9th Asia and South Pacific Design Automation Conference (ASP-DAC)*, pp. 73-78, 2014.
- [8] Y. R. Cao.Y, "Optical identification using imperfections in 2D materials," 2017.
- [9] Missous et al., "Fabrication of Submicrometer InGaAs/AlAs Resonant Tunneling Diode Using a Trilayer Soft Reflow Technique With Excellent Scalability," *IEEE electron device Letters*, vol. 61, no. 7, 2014.
- [10] U. I. Bagci, "Generating Secrets From Quantum Confinement Physically Unclonable Functions," *In Press.*, 2016 .
- [11] M. o. c. a. IT, Fingerprint image and Minutiae Data Standard for e-Governance Applications in India, 2010.

Chapter 2- The Physics of Semiconductors and the QCPUF.

[2.1 Introduction](#)

We begin by drawing our attention to a brief summary on the physics of semiconductors and in particular how we utilise the phenomena of solid state structures to create entities such as tunnel diodes. In this chapter we will elucidate how quantum effects in semiconductor nanostructures can be exploited in cryptography in the form of a quantum confinement physically unclonable functions (QCPUFs) and provide the argument of how we are able to increase its bit density.

Central to our investigation is the resonant tunneling diode (RTD), a heterostructure that functions based on quantum tunneling. In particular it is the minute imperfections within the bandgap, interfacial roughness and doping profile of these semiconductors that yield the significant elements of our research. To reiterate as previously expressed; we are making use of atomic imperfections as a means of identification analogous to that of our fingerprint.

Although we do not contribute to any new theoretical discussions, we present the prerequisite literature to support our experimental findings later. We begin by reviewing the topic of the quantum theory of heterostructures, the effect of quantum confinement, band structure, the density of states and quantum tunneling. We will describe the roles of the semiconductor in our investigation and study the structure of quantum wells (QWs) and their application to double barrier resonant tunneling diodes (DBRTD) and their epitaxial growth. Furthermore we present the theoretical argument behind how physically altering such a structure will give rise to additional minutia and reference the initial studies of Reed et al.

[2.2 Band structure, doping and III-V semiconductors](#)

Our devices are primarily comprised of materials known as semiconductors, such materials exhibit useful properties in that at room temperature they are electrically conducting however they differ to regular conductors such as copper or zinc in that at absolute zero they in theory are completely insulating.

We recall that the outermost orbital structure of an atom consists of a lowest unoccupied molecular orbital (LUMO) and the highest occupied molecular orbital (HOMO), otherwise known as the conduction band and the valance band respectively. In conductors, these such bands overlap allowing for electronic and thermal transport. In particular our devices are comprised of elements that exist in groups III and V of the periodic table, such semiconductors are hence often referred to as III-V semiconductors, others such include III-Nitride and II-VII.

The electronic energy bands are intervals in which electronic states occupy, the tight binding model allows a general framework on the origin of electronic bands in crystal structures which we summarise as follows: The effects of quantum mechanics renders electrons in a solid to experience periodic potentials caused by the atom's crystal lattice. The dispersion relation of an electron in a lattice highlights such quantisation, however the periodic potential in a typical crystal structure alters the

dispersion relation of electrons. Namely when the wavelength of the electrons propagating through the lattice is comparable to the lattice spacing $k=\pi/a$ where k is the wave vector and a is the lattice spacing. In particular the electrons are reflected due to the varying potential of the lattice and form standing waves of different displacements by $a/2$. As a result, these standing waves have different energies known as bands, the spacing between these bands are termed bandgaps and are prominent in insulators and semiconductors. The highest energy band with the most occupied states is referred to as the valence band whereas the lowest energy band with least occupied states is the conduction band. Semiconductors host a bandgap minimal compared to that of insulators, electrons can be thermally excited from the valence band to the conduction band and are governed by Fermi-Dirac statistics. However at absolute zero the semiconductor behaves as an insulator as there exists no free electrons, the Fermi level is the highest energy occupied by electrons in a material at 0K.

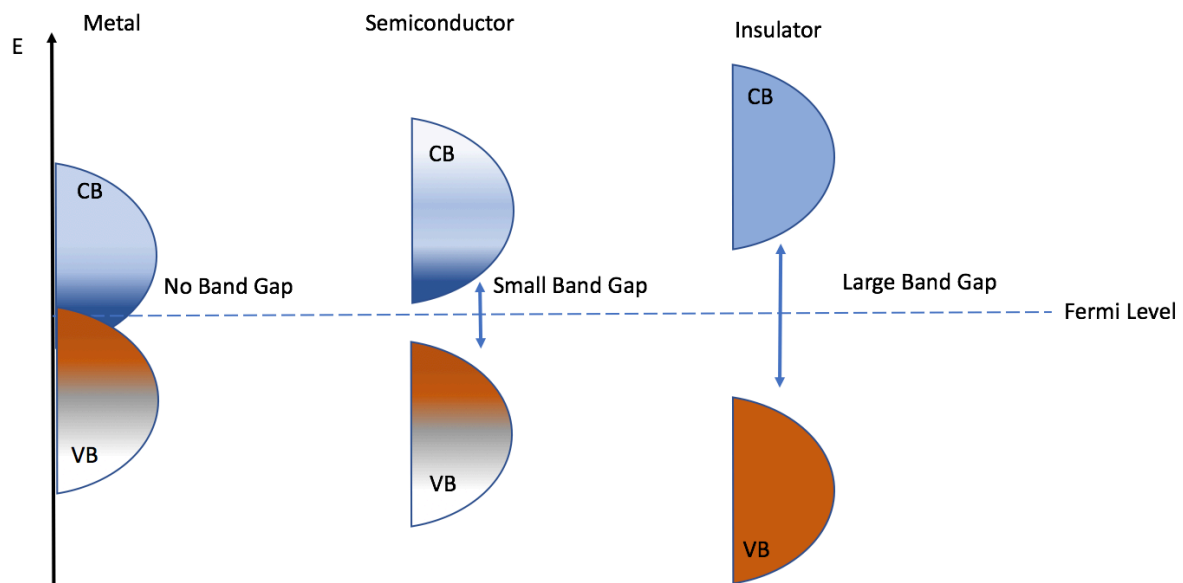


Figure 2.1: Variation of bandgap in metal, semiconductor and insulator highlighting the conduction and valence bands. Insulators having the largest bandgap followed by semiconductors than metals.

2.3 Doping and Fermi level pinning

The intrinsic properties of semiconductors can be altered by introducing impurities, this process is known as doping and exist in two types of dopants: donors and acceptors. The elements used depend on the host material; acceptors are dopants that contain fewer electrons than the hosting material (p-type) and whereas donors are atoms that contain a greater number of electrons than the hosting material (n-type). With these subsequent doping types, acceptors typically have an unoccupied energy level (acceptor level) that is positioned above the valence band and donors have an unoccupied electron level that is positioned below the conduction band.

The position of such bands allows for variations in conductivity [2], when slight changes in doping concentration (or other sources of carriers) induce surface states in the bandgap, electrons from the valence band are trapped in these states and until such overlaps with the Fermi level. This causes changes in the Fermi level and is referred to as Fermi level pinning. Such can lead to decreased

conductivity and can be due to surface effects, i.e. caused by the exposure to a gallium ion beam on the heterostructure surface.

2.4 Density of states: quantum wells, wires and dots

We have thus far briefly touched upon the effects of quantisation and how such influences the formation of bands, however quantum confinement influences the bulk properties of the material in particular that the bandgap increases as the dimension of our sample decreases. We observe such effects when the physical dimensions of our system is of the order of the de Broglie wavelength.

$$\lambda = \frac{h}{(m^*k_B T)^{1/2}} \quad (1)$$

Where k_B is the Boltzmann constant, m^* is the effective mass of the electron, h is Planck's constant and T is the temperature. The application of such in different structures is also of central importance in our understanding of how RTDs work. We classify structures based on their degree of confinement;

Three dimensional structure (bulk):- The dimensions of the structure are large such that there exhibits no confinement in any directions

Two dimensional structure (quantum well):- Confinement exists in one dimension (z) and the electrons are free to move in the x & y planes .

One dimensional structure (quantum wire):- Confinement exist in two dimensions (z, x) and the electrons are free to move in the y plane.

Zero dimensional structure (quantum dot):- Confinement exists in all three dimensions (x, y, z).

The order of confinement occurs (Fig 2.2) when the dimension of our structure is comparable to the de Broglie wavelength of the electron, also known as quantum box quantisation.

The Schrödinger equation which describes our system is extremely difficult to solve analytically, in particular when dealing with our system of heterostructures; approximate methods such as perturbation theory, quantum Monte Carlo, WKB approximation, etc. are the only means of solving such. The density of states (DOS) is defined as the number of allowed states within energy range. A general derivation for DOS in multiple dimensions is found in [1], however for convenience we present the subsequent dispersion relation for all four cases (Bulk, 2D, 1D, 0D).

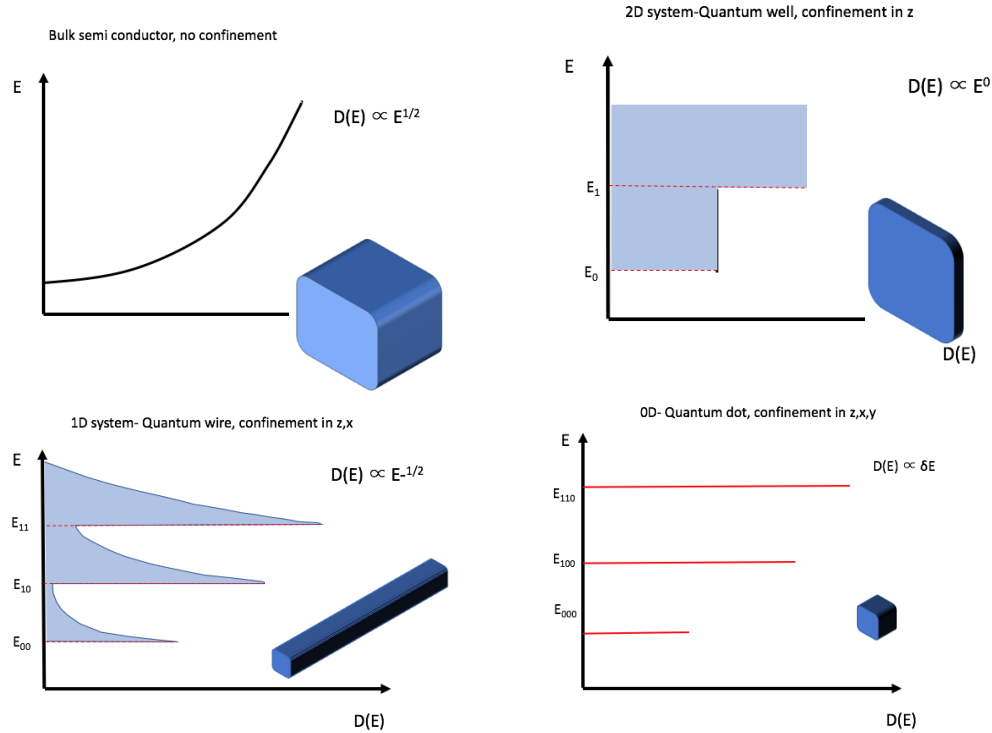


Figure 2.2: Energy vs density of states (DOS) of 3D system (bulk), 2D (quantum well), 1D (quantum wire) and 0D (quantum dot) systems. The inset highlights the planes of confinement.

Given we are able to contrast and compare the different levels of confinement by comparing their density of states vs their confined states. If we now confine electrons in an additional dimension such that the electrons are restricted in two dimensions and are free to move in one we have effectively created a quantum wire structure. Further confinement to a third degree, now reducing the dimensionality of the free electron to zero creates a structure known as a quantum dot. A material that does not exhibit confinement in any dimension is simply referred to as the bulk and exhibits no quantum effects.

Structure	Degree of Freedom	Nanoscale dimension	Density of States
Bulk	3	$1\mu\text{m} \rightarrow \infty$	$DOS_{3D}(E) = \frac{8\pi\sqrt{2}}{h^3} m_{DOS}^{3/2} \sqrt{E - E_c}$
Quantum Well	2	1-1000 nm (thickness)	$DOS_{2D}(E) = \frac{4\pi}{h^2} m_{DOS}$
Quantum Wire	1	1-100 nm (radius)	$DOS_{1D}(E) = \frac{2\sqrt{m_{DOS}\sqrt{2}}}{h\sqrt{E}}$
Quantum Dot	0	1-10 nm	$DOS_{0D}(E) = 2\delta(E - E_c)$

Table 2.1: Order of magnitude to induce quantum confinement in different dimensions, the expressions of the DOS give rise to the features observed in Fig 2.2.

A quantum well structure can be replicated when combining a material of a wider band gap (i.e. GaAs) followed by a material of a narrower band gap (i.e. InGaAs) followed by the wider band gap material again; in our case a sandwiched layer of indium gallium arsenide (InGaAs) between two layers of aluminium arsenide (AlAs) was studied. The details of the fabrication method are discussed later in Sec 2.5, the growth of this heterostructure in the Z direction then forms a quantum well where electrons experience quantum confinement. The laws of quantum mechanics renders the electron subjected to confined subbands that are of discrete energy. The electron is still free to move in two other dimensions and behaves as it would in a two dimensional electron gas.

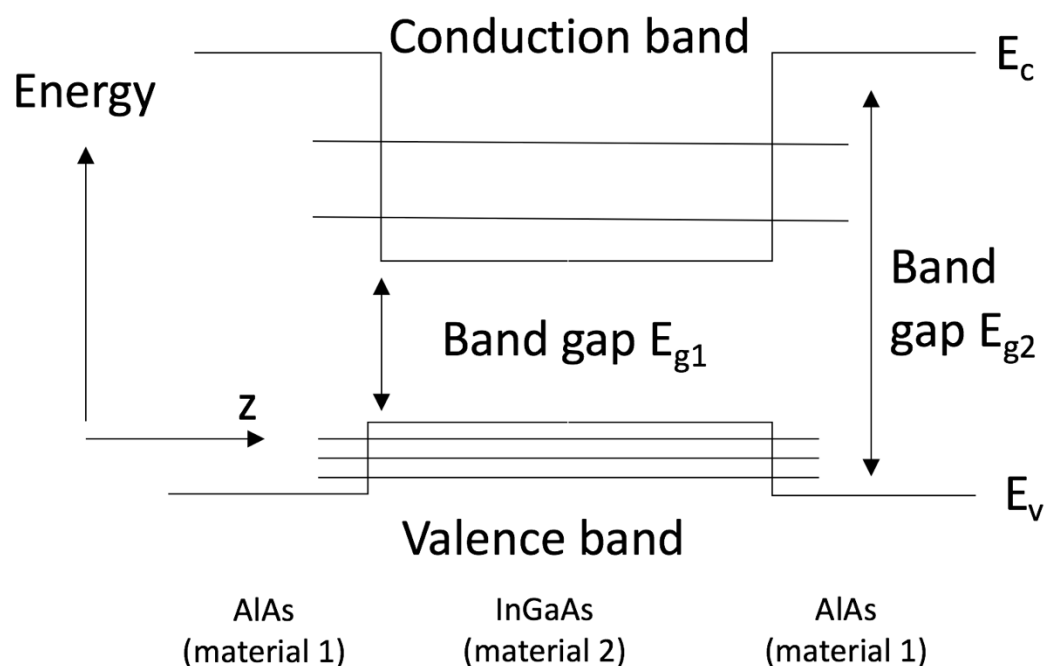


Figure 2.3: 2D confinement AlAs/InGaAs/AlAs quantum well showing the confined levels in the valence and conduction band. The rectangular shape is due to the perfect epitaxial growth.

Much of our attention will be centred on the quantum well, advancements in heterostructure engineering have enabled devices that utilise the effects of quantum confinement in the production of resonant tunneling diodes [3].

[2.5 The resonant tunneling diode](#)

We have demonstrated that quantum wells are the simplest of structures to exhibit quantum confinement. We now draw our attention to a particular diode that makes use of the property quantum tunneling in which the wave function of an electron has some finite probability that enables it to enter into a forbidden region due to its wave-particle characteristics. Tunnel diodes exhibit a characteristic negative differential region (NDR), the RTD follows a structure similar to that of Fig 2.3, in which material 1 forms the barriers and material 2 forms the well of confinement.

As a potential difference is applied to the structure charge accumulates at the conduction band and very little current pass through (tunnels) the potential barrier. Upon increasing the voltage, a Stark shift causes the region of charge (Fermi level) to approach the first confined state in the well, this increases the tunneling probability until the conduction band comes in line with the confined state

and resonates allowing the maximum rate of tunneling. Further increasing the voltage results in the first confined state becoming lower in energy and enters the region of the bandgap, transmitted current degrades. However further increasing the voltage will allow thermionic means of electrons to transmit.

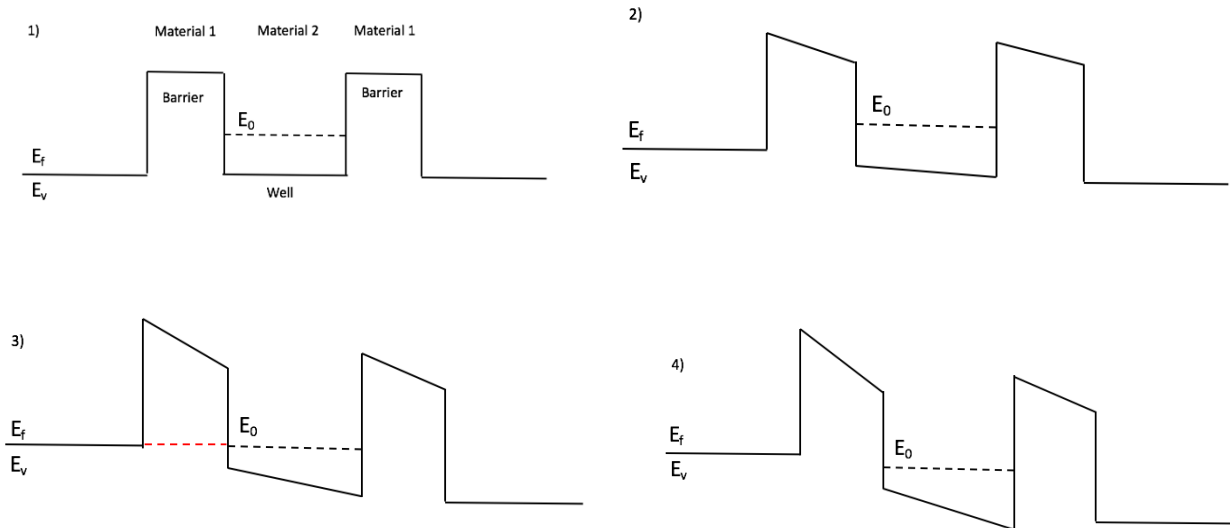


Figure 2.4: Representation of the resonant tunneling process where a bias is applied and causes a shifting in the bands. 1) shows the structure at zero bias, 2) with some applied bias, 3) the Fermi sea coming in line with the first confined state 4) thermionic means of conduction occur.

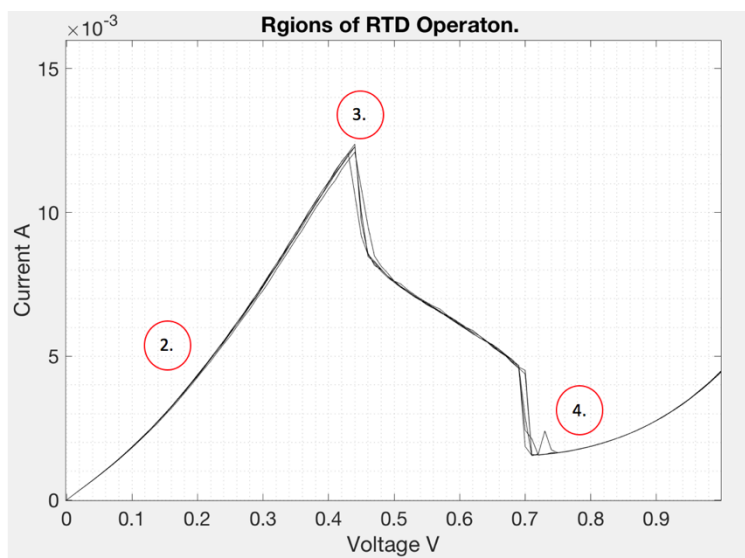


Figure 2.5: IV characteristic of a RTD undergoing a bias highlighting the different stages of resonant tunneling, where voltage is sourced and current is measured.

The NDR region is the sources of much research on the devices, as a result of such a feature they can be used as oscillation devices reaching frequencies of the terahertz [4].

2.6 Fabrication of the RTD

RTDs have been studied for decades, they were first discovered by [3], since then many groups have fabricated them using a wide variety of methods such as via reactive ion etching and electron beam lithography. The different methods vary in complexity and resources. The devices were fabricated by Missous et al. using a trilayer soft reflow method [5] which uses photolithography to laterally define the structure. The structure was grown in a RIBER V1000 molecular beam epitaxy (MBE) on an indium phosphate substrate.

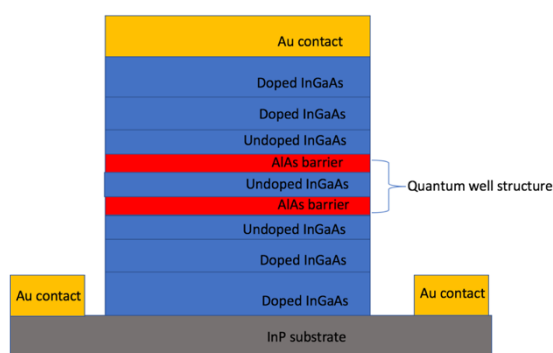


Figure 2.6: Schematic of RTD structure showing epitaxial arrangement and positioning of contacts.

Layer	Thickness (nm)	Doping (cm^{-3})
InGaAs(n+)	45	$2.00\text{E}+19$
InGaAs(n-)	25	$3.00\text{E}+18$
InGaAs	20	undoped
AlAs	1.3	undoped
InGaAs	4.5	undoped
AlAs	1.3	undoped
InGaAs	20	undoped
InGaAs(n+)	25	$3.00\text{E}+18$
InGaAs(n-)	400	$1.00\text{E}+19$
InP substrate		

Table 2.2: Thickness and doping profile of structure, highlighting doped and undoped region [5].

It has been shown that monolayer variations in AlAs barriers yield a variation of 270% in the IV characteristics of RTDs [5]. Such variations are extremely difficult to govern and are often induced in the fabrication stage, additionally the position of the confined states are sensitive to the quantum well width, barrier height and well depth. When considering our heterostructure and their atomic make up, it is considered extremely infeasible to identically replicate two RTDs to near perfection [6].

2.7 The PUF, QCPUF and RTD

In this section we expand on the previously introduced concept of a physically unclonable function (PUF), we will also reveal how many of the fundamental concepts explored above can be exploited and used as a PUF. The notion of a PUF was initially introduced by Pappu et al. [8]. In the original publication it described that a PUF must be a physical unit that can be evaluated at great ease but impossible/infeasible to replicate despite infinitely advanced computational capabilities. Analogously one can view the PUF as a physical analogue of a mathematical one way function.

At the heart of every PUF is randomness, such can come in different forms and is paramount that under different conditions each PUF stays unique to itself. There exist PUFs who's randomness can be explicitly induced by controlling and optimising specific parameters, such PUFs include optical PUFs and coating PUFs. There also exist PUFs that rely on intrinsic randomness. It has been previously suggested that other quantum systems can be used as PUFs, such as quantum dots [9]. Defects and disorder induced in the fabrication process can be observed when studying the variations in the optical spectra. Further detail of the mechanics of extracting the optical spectra from quantum dots for their use as a PUF can be studied in [6]. Recently it has been shown by Roberts et al. [9] that the resonance peak position of the IV characteristic of RTD can be utilised as such PUF. As mentioned above the fabrication process induces uncontrollable minute variations within the heterostructure. In Roberts' work they investigated the uniqueness of such QCPUF and found little to no similarity of two RTDs.

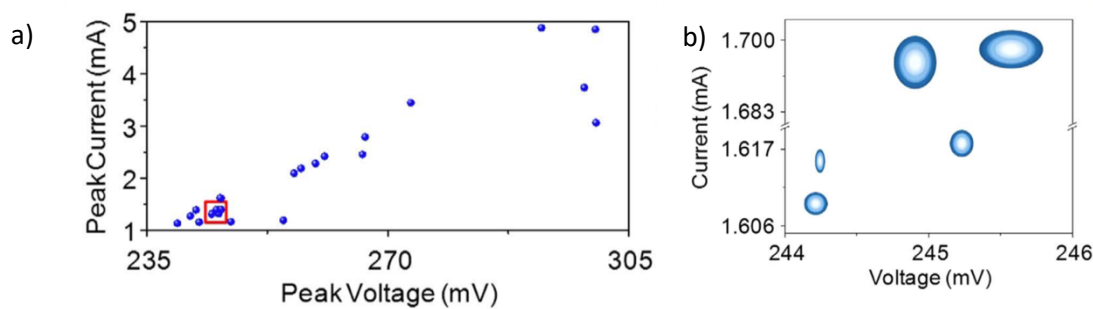


Figure 2.7: (a) Different peak position of 26 identically manufactured devices showing a clustered region encircled in red. (b) Confidence regions of peak position from clustered region in (a). Inner most radius refers to 95%, middle region refers to 99.99% and outer most region refers to 99.997%. Taken from [9] with permission.

Further studies have shown that the QCPUF is extremely robust and can be a source of reliable uniqueness. The following section will review the suggested implementation of such.

[2.8 The case of the strong PUF vs the weak PUF](#)

UOs have been implemented on currency notes and documents of ID, however such can be more versatile and can be implemented in a wide range of applications such as key/random number generation. One method used in verifying a PUF is known as the challenge response pair (CRP); such requires the use of a secure database to host the exact CRP and to provide unique yet repeatable responses to the challenges.

Every CRP must be removed from the database after each use, the question of the security of such database is reserved for another study. Nonetheless another scheme suggests the use of a single CRP that rather than requires the use of a database, uses a certificate verified and hosted by the manufacturer [11]. PUFs also known as physically obfuscated keys (POKs) are a good example of a weak PUF. Both types of PUFs can be used in such a way that the responses are used in key generation and must abide by the CRP protocol such that in response to every challenge an output is generated that is unique and randomly dependant on the internal structure. Both PUFs are ideally stable under different moderate environmental conditions. Ideally a weak PUF is kept secure through implanted hardware and generate keys from a select number of CRP that is able to scale polynomially. A strong

PUF however allows an attacker to gain access to the PUF and to apply as many challenges and record as many responses as they wish. However the attacker will have a near impossible chance at predicting the response for every given challenge even providing the attacker has sufficient amount of time due to the exponential nature of the complexity of the PUF.

Currently the QCPUF relies on the resonance peak position which has strong evidence backing its uniqueness which relies on confinement in one dimension, however to increase the complexity (and to increase the bit density) of our PUF we propose increasing the dimensionality of confinement to induce further resonance peaks that by deduction will be just as unique as they rely on similar mechanisms and conditions (i.e. atomic scale variations).

In [12], Bagci's outlined a scheme of extracting binary information from such physical systems from their peak position. A Gaussian peak finding algorithm locates the peak position and divides the current and voltage axis into bins (Fig 1.3a). Each respective bin contains binary information and scales as the number of bins increase (Fig 1.3b). Per device the optimum number of bits extractable without influence of measurement fluctuation was $k=256$, such outputs 8 bits from the relationship

$$b = \log_2(k) \quad (2)$$

where b is the number of bits and k is the number of bins. To obtain the more optimum 128 bits, Bagci followed a method of concentration where the total number of bits B (128) depends on the number of devices (φ) and how many individual bits we are able to extract from each device, while keeping k constant (256); as $\varphi = B/b$. From this it can be deduced that using an 8 bit sequence would require 16 concatenated devices, and a 6 bit sequence would require 22 devices.

2.9 Resonant tunneling through higher order states

As we have pointed out previously, decreasing the physical dimensions of our bulk sample restricts the degrees of freedom of our electrons and induces confinement in other dimensions. A RTD visualises confinement in the 2D case, however in theory it is possible to visualise electron tunneling as a series of multiple resonant peaks in the 1D and 0D case by confining our system [12]. such gives rise to multiple resonance peaks visible within the IV spectrum. However to justify such an argument we reference the works of Reed Et al, S.Tarucha and M.Van Hove Et al. who conducted similar studies with different structures and for different applications. Their work nonetheless demonstrated the effect of resonant tunneling in 0D and 1D. Their results demonstrated clearly that their bumps were the result of lateral constriction of their heterostructures. Detailed theoretical descriptions concerning the underlying mechanisms were brought forward in subsequent publications. However Issues arise when modelling 0D tunnelling such as lateral mode mixing which varies on the uniformity of the confinement potential and the mixing of resonant tunnelling and Coulomb blockade single electron tunnelling effects.

The initial study by Reed et al. [12] fabricated narrow columns of AlGaAs/InGaAs and observed a series of resonant peaks attributed to RT in 0D. Observation of 0D states in AlGaAs-GaAs heterostructures laterally constricted by hydrogen plasma [11] present aligning results to Reed's work.

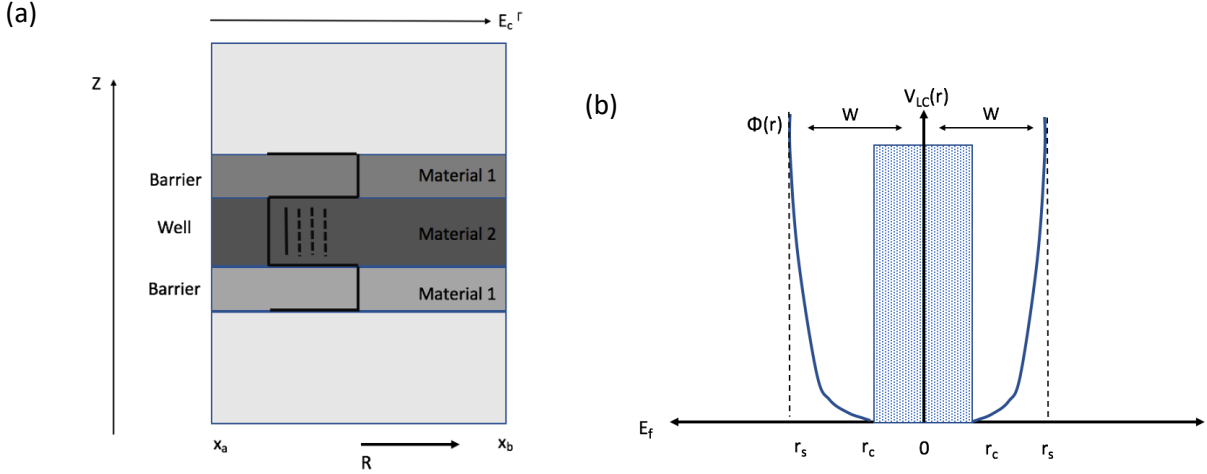


Figure 2.8: (a) Representation of epitaxial structure containing a quantum well hosting multiple confined states due to OD confinement, E_c^Γ is the gamma point conduction band, R is the radius of the column. (b) confinement potential of a laterally constricted column, $V_{LC}(r)$ is the laterally confined potential. W is the depletion depth, the blue shaded region is the effective channel [14].

In Reed's work electrons are laterally confined to a 'gutter' potential which is comprised of a flat and parabolic region. The fine peak structure found in Reed's and in other cited work [12] were only visible at low temperatures.

A difficulty in modelling the behaviour of OD tunneling stems from the non-uniform lateral confinement potential such results due to the lateral quantised energies varying steeply in the z dimension of the quantum dot. This is because the spacing of energy bands in the well is much greater than in the contact (emitter) region. In addition to this, the uneven confinement causes lateral-mode mixing of the wave functions. It was found by Reed et al. that the fine peak structure observed in the IV characteristic can be modelled as resonances of confined states within the well aligning with those in the emitter (conduction band). In Reed's work the potential of the OD structure was given by

$$\Phi(r) = \Phi_T \left[1 - \frac{R-r}{W}\right]^2 \quad (3)$$

Where r is the radial coordinate, R is the radius of the lateral column, Φ_T is the potential height, W is the depletion depth. The authors also resolve the splitting of the quantised electron states as

$$\Delta E = \frac{\hbar}{R} \sqrt{\frac{2\Phi_T}{m^*}} \quad (4)$$

Where m^* is the effective mass in the well. Their measured value of state splitting is 25meV and matches closely with their expected value of 26meV.

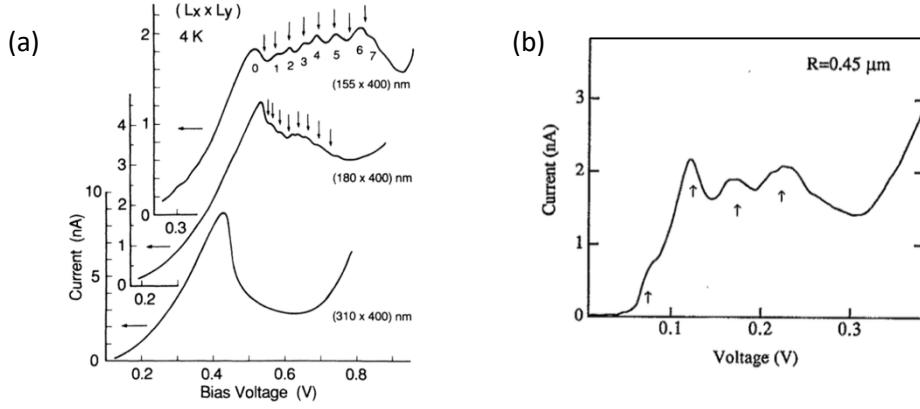


Figure 2.9: (a) Peaks in NDR region which correspond to tunneling through discrete states in the 1D & 0D structure measured at 4K. The arrows correspond to the calculated voltage positions of each state. Reprinted from [14] (b) Fine structure attributed to quantum box quantisation measured at 1.2K, where R is the varying diameter of the emitter contact. Reprinted from [13].

2.10 Temperature dependence of bandgap

Central to our clarification is studying the effect of temperature on semiconductor heterostructures. We conduct cryogenic measurements and observe changes of the peak and valley position. We also observe the prominence/broadening of such bumps within the NDR (Sec 4.3.5). Although a more rigorous theoretical evaluation of the effect of temperature on semiconductors is beyond the scope of this thesis. We briefly illustrate said effect by introducing Varshni's empirical formula which highlights the increase in bandgap energy with decreasing temperature. The formula is dependent on two constants (α and β), specific to the element that determine the relationship of bandgap energy and temperature.

$$E_g(T) = E_g(0) - \frac{\alpha T^2}{T + \beta} \quad (4)$$

Where $E_g(0)$, α and β are fitting parameters dependent on the material.

	Si	Ge	GaAs
$E_g(0)$ (eV)	0.7437	1.166	1.519
α (eV/k)	4.77E-4	4.73E-4	5.41E-4
β (k)	235	636	204

Table 2.3: Material constants for Varshni's empirical formula, for Silicon, Germanium and Gallium Arsenide [13].

One can comment that at lower temperatures, the amplitude of atomic vibrations decrease which causes a smaller interatomic spacing and follows a trend seen in Fig 2.10.

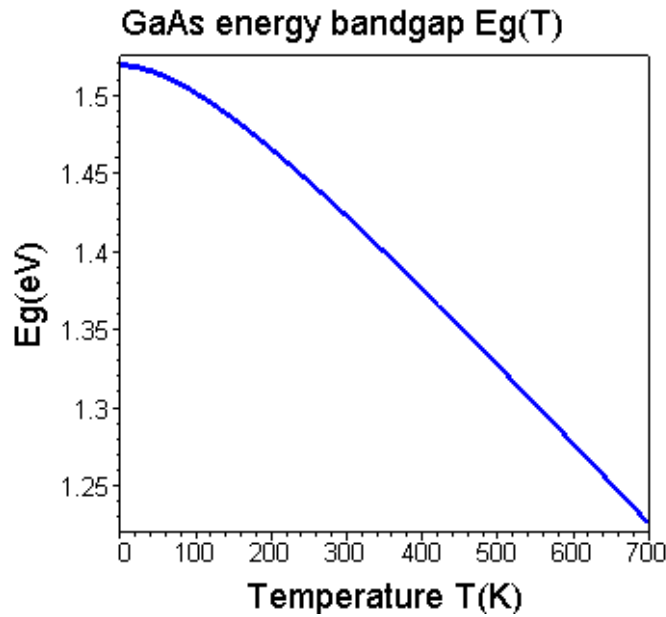


Figure 2.10: Variation of bandgap of GaAs with temperature showing an increase in bandgap as temperature decreases [16]

Thus far we have described crucial theoretical aspects to the underlying physics of semiconductors and the RTD. We've outlined how by engineering and utilising variations in bandgaps we are able to create physical structures that host a quantum well. It has been shown that uncontrollable factors during the fabrication process renders no two devices alike and hence by utilising the position of the confined states within the wells we are able to use the IV spectrum of the RTD as a UO. However currently we rely on the peak position as our source of uniqueness, we have proposed the concept of physically altering the structure to induce more peaks (as a method of increasing the bit density) and referenced previous studies that demonstrate the same concept but with other heterostructures. In the following chapter we approach our main aim by describing the experimental methods we employed to reach said goal.

Bibliography

- [1] C. S. H. & V. A. Johnson, "Resistivity of Semiconductors Containing both Acceptors and Donors," *Phys. Rev*, vol. 79, no. 535, 1950.
- [2] T. Heinzl, *Mesoscopic Electronics in Solid State Nanostructures*, 2 ed., Wiley-VCH, 2007.
- [3] L. R. Tsu, "Tunneling in a Finite Superlattice," *Appl. Phys. Lett*, vol. 22, no. 562, 1973.
- [4] K. J. P. J. e. al., "A Dual-pass High Current Density Resonant Tunneling Diode for Terahertz Wave Applications," *IEEE Electron Device Letters*, vol. 36, no. 12, 2015.
- [5] e. a. M. Missous, "Fabrication of Submicrometer InGaAs/AlAs Resonant Tunneling Diode Using a Trilayer Soft Reflow Technique With Excellent Scalability," *IEEE electron device Letters*, vol. 61, no. 7, p. 2014.
- [6] J. e. a. M. Missous, "Extremely Uniform Tunnel Barriers for Low-Cost Device Manufacture," *IEEE ELECTRON DEVICE LETTERS*, vol. 36, no. 6, 2015.
- [7] M. K. e. a. C. Shao, "Achieving reproducibility needed for manufacturing semiconductor tunnel devices," *IEEE Electronic Letters*, vol. 49, no. 10, 2013.
- [8] R. e. al., "Physical One-Way Functions," *Science*, vol. 297, no. 5589, p. 20262030, 2002.
- [9] J. e. a. Roberts, "Using Quantum Confinement to Uniquely Identify Devices," *Nature Scientific Reports*, vol. 5, no. 16456, 2015.
- [10] A. Elliott, *The effects of quantum dot nanoparticles on the PolyJet direct 3D printing process.*, Virginia Polytechnic Institute and State University, 2014.
- [11] U. I. B. e. al., "Generating Secrets From Quantum Confinement Physically Unclonable Functions," *In Press*, 2016.
- [12] P. L. J. R. A. V. C. & W. W. Koeberl, "A practical device authentication scheme using SRAM PUFs," in *The 4th International Conference on Trust and Trustworthy Computing*, 2007.
- [13] M. A. R. e. al., "Observation of Discrete Electronic States in a Zero Dimensional semiconductor Nanostructure," *Physical Review Letters*, vol. 60, no. 6, 1988.
- [14] M. H. e. al., "Zero-dimensional states in submicron double-barrier heterostructures laterally constricted by hydrogen plasma isolation," *Journal of Applied Physics*, vol. 72, no. 158, 1992.
- [15] T. e. al., "Resonant tunneling through one- and zero-dimensional states constricted by Al Ga — As/GaAs/Al Ga — As heterojunctions and high-resistance regions induced by focused Ga ion-beam implantation," *Physical Review B*, vol. 41, no. 8, 1990.
- [16] B. V. Zeghbroeck, "ecee.colorado.edu," University of Colorado, 1997. [Online]. Available: <http://ecee.colorado.edu/~bart/book/eband5.htm>. [Accessed 04 8 2017].
- [17] B. Optoelectronics, "Energy Band Gap E_g of GaAs," [Online]. Available: http://www.batop.com/information/Eg_GaAs.html. [Accessed 04 8 2017].
- [18] M. J. Kelly, "New Statistical Analysis of Tunnel Diode Barriers," *Semicond. Sci. Technol*, vol. 15, 2000.

Chapter 3- Experimental methods.

3.1 Introduction

Thus far we have outlined in theory not only the underlying physics of semiconductors but of what we require in order to increase the bit density of the QCPUF. In practice a number of experimental methods in the modification and characterisation stages require a detailed explanation. In this section we will explore the means in which we conducted such, beginning with how we optically pre-characterised our devices with the use of scanning electron microscopy, then discuss how we modified our devices with the focused ion beam. We examine our means of electrically testing and studying their IV characteristic under different temperatures, highlight the problems we encountered and raise a number of issues that would be addressed in future studies.

3.2 Scanning electron microscopy

As the typical dimension of the RTDs are on the order of micrometres; an optical microscope with an objective lens of x100 is insufficient to observe the details of the etching process or any heat damage due to the thermal resetting of the RTDs (~100 nm). For this reason, the scanning electron microscope (SEM) was used to observe such features and at times in combination with a focused ion beam (FIB). The SEM employs a raster scan by using focused electrons across a rectangular area of the sample and relies on electrons as opposed to photons. Information on the surface topography is obtained from the electrons bouncing back from the surface of the specimen in addition to any heat, backscattered/secondary electrons emitted from the surface.

Information on the material composition can also be obtained when electrons ionise and emit x-rays from the specimen surface [1]. The scanning electron microscope is considered a non-destructive process and specimens can be analysed repeatedly, however the vacuum may cause some samples to outgas which rules out many organic compounds (i.e. hydrocarbons).

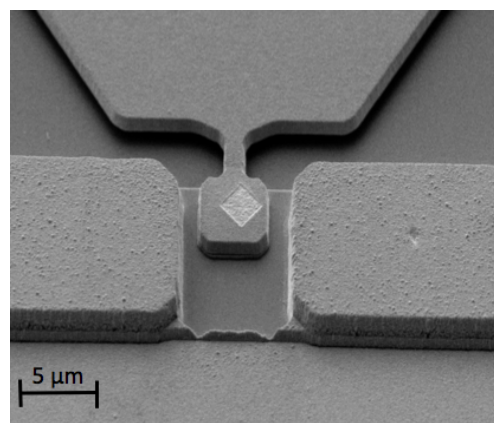
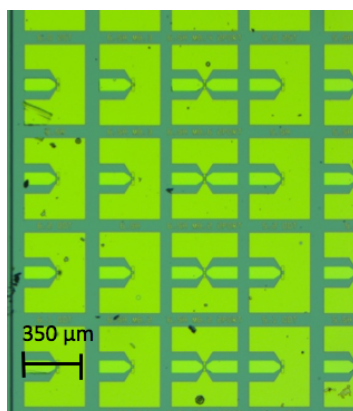


Figure 3.1: (Left) optical microscope image of RTDs at 50x. (Right) SEM image of single device RTD.

3.3 Focused Ion Beam

An effective means of etching at a high level of precision and accuracy was with the use of a focused ion beam (FIB). FIB technology has enabled the development of scanning probe tips [2] mask less FIB lithography [3] and many other advancements in the area of nanofabrication, the FIB was housed in a class 100 cleanroom in the IMDEA Nanoscience Institute in Madrid. We employed a dual FIB-SEM system, in addition to the Ga^+ reservoir (beam source), an electron beam was used as a SEM to image the sample and provide accurate milling or deposition of materials with high resolution imaging. However imaging with low Ga ion beam currents (30-50pA) is feasible but at much lower resolutions and can degrade the sample, the FIB can also be used as a means of deposition.

The dual FIB-SEM beam had a working distance of 5mm, the standard FIB commonly uses a liquid metal gallium ion source due to its low melting point ($\sim 300\text{k}$), low volatility, unreactive nature and its vacuum properties, additionally gallium is preferred for milling due to its weight. When the gallium is heated such that it forms a liquid metal ion source (LMIS), it is focused on a tungsten needle tip. The LMIS forms what is known as a Taylor cone due to an external electric field and the surface tension of the liquid Gallium, which occurs when the gallium is subject to an electric field. As the electrostatic field is increased field emission of the ions occurs and the ions are subsequently focused by an electrostatic lens. As the ions are directed to the surface of the sample sputtering of the sample takes place and the sputtered ions and their corresponding electrons leave the surface and are able to form an image similar to that used by an SEM. The resolution of the FIB is limited to 5nm by the mentioned sputtering process (at low powers).

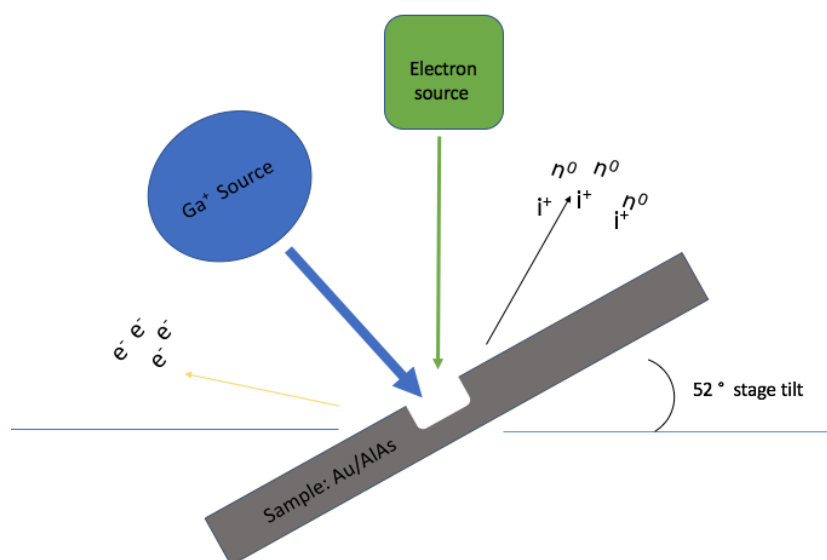


Figure 3.2: Schematic of a typical dual beam (FIB-SEM) in a chamber configuration. The sample is positioned 52° normal to the ion beam source. The Ga ion induces secondary electrons (e^-) as well as secondary ions (i^+) or neutral atoms (n^0). The electron source allows for microscopy.

A challenge that arose in using the dual FIB-SEM was calibrating the concentric axis where both the FIB and SEM lay. The initial calibration process required that we applied a low FIB beam current to etch a visible mark on the sample to gauge where the ion beam would mill. Repositioning the stage to mill subsequent other devices requires that we repeat this step to gauge to a better degree (although still approximate) the exact location of where the milling will take place. This was often an inaccurate and time consuming method as we regularly encountered that our ion beam was a few hundred nanometres off, the results were FIB etches that would produce RTDs with isolated active regions and asymmetric cavities. Figure 3.3c highlights a case where poor alignment and inaccurate gauging resulted in a device with less laterally confined active regions than aimed.

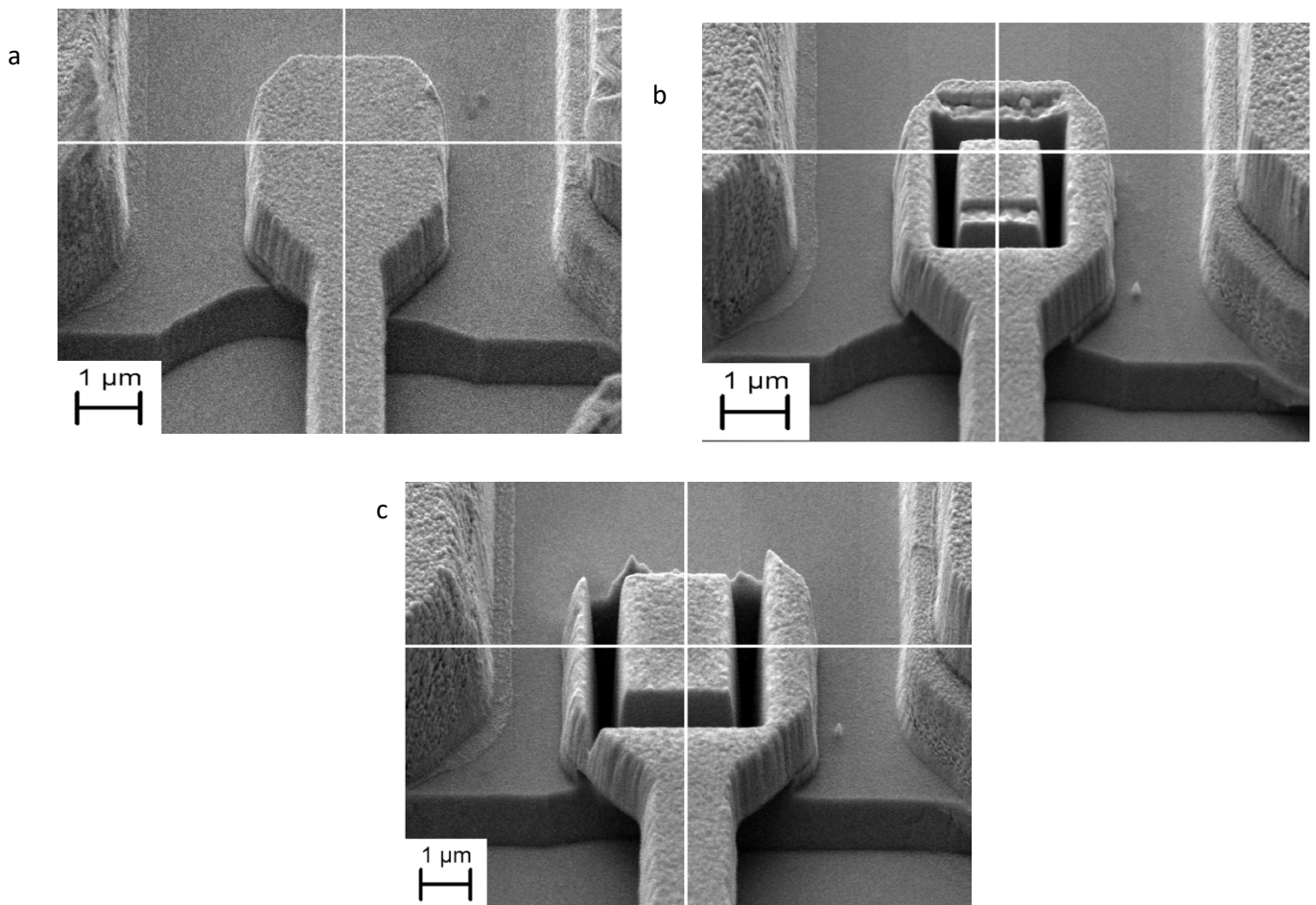


Figure 3.3: (a) SEM image of a 3x3 μm sized mesa RTD prior milling. (b) A device post milling with FIB with four laterally confined active regions. (c) 4x4 μm sized mesa RTD with Poor alignment of ion beam stencil on the sample results in imperfect etch cavity on the mesa.

3.4 Electronic characterisation

Prior to any modification to our devices we required a full electronic characterisation, we measured current-voltage spectrums (IV curves) of our devices under both bias; before and after modification and under low temperature to observe interesting features. By applying a voltage sweep we recorded subsequent values of current, in each case we relied on a source measure unit (SMU) to source the

desired input voltage and measure the output current. Regardless of our setup and our desired environment (i.e. low temperature/room temperature).

3.4.1 Source measure unit

The SMU (Keithley 2400) is an electronic instrument that can be used to both source and measure electronic components simultaneously, it allows for high precision characterisation of electronic components. We resorted to a python script written by R.Bernardo-Gavito that would source voltage and measure current, the script allowed us to vary the measurement resolution and basic sweeping parameters such as compliance and initial and final voltage values. In our setup we employed a sourced delay measurement cycle; following an applied voltage a delay time is induced to allow the source to reach the desired value (dependent on the capacitance of the internal circuitry of our RTDs) which we set to 50ms based on the previous suggestion and work by J.Roberts. Power line induced AC noise can inhibit measurement resolution however by allowing an increased AC line integration time for our measurements we can increase the resolution of our measurements; a trade-off is reduced measurement rate. We set our NPLC value to a recommended 0.05.

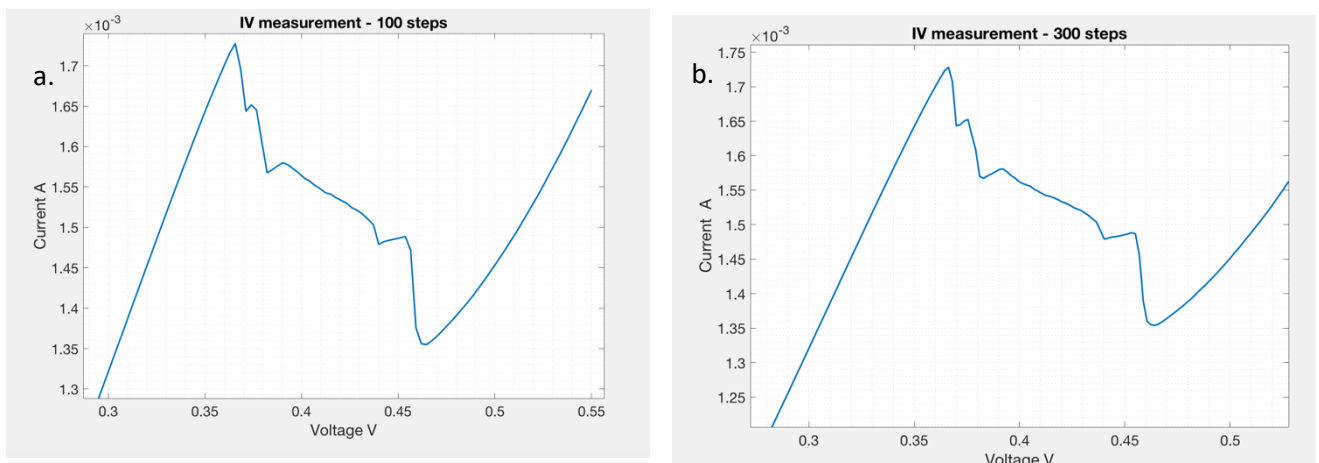


Figure 3.4: (a) IV characteristic of a RTD taken with a 100 step resolution. (b) IV characteristic of a RTD taken with a higher 300 step resolution showing little observable difference.

The number of steps determined how many individual points of data were plotted. 100 steps were sufficient in producing a detailed IV spectrum however in many cases we resorted to a higher resolution of 400. A fixed current compliance was kept which prevented an overload of current, the value of such varied depending on the device size as different RTD devices reached resonance at different currents (Fig 1.2).

3.4.2 Room temperature probe station

A mechanical probe station (Wentworth Lab MP2010) was used to obtain characteristic measurements of semiconducting devices. Manipulators allow precise positioning of tungsten needles to allow electrical stimulation and in many cases, can incorporate cryogenic conditions. Tungsten probes with an average radius of 1 μm , we assume negligible resistance from the probes and hence rely on a 2-terminal sensing setup. The nature of the size of samples examined with a probe station necessitates a microscope to allow for fine positioning of the probes. An advantage of the mechanical probe station is the efficiency in characterisation, given an average characterisation time of

approximately five seconds, we are potentially able to measure hundreds of devices per hour assuming parameters (i.e. compliance) remain constant. The process of repositioning the probes and sample requires little time.

However repeated measurements on the probe station induced aggravated contact damage (Fig 3.5), such increased the likelihood of unstable readings due to discontinuities and current fluctuations. In addition to the afore mentioned issues; the probe station used was subject to vibrations from an unknown source, due to the size and weight of the probe station relocating such was infeasible. External vibrations yielded inconsistent measurements, nevertheless we in our case we found vibrations to be negligible when the sample was repositioned.

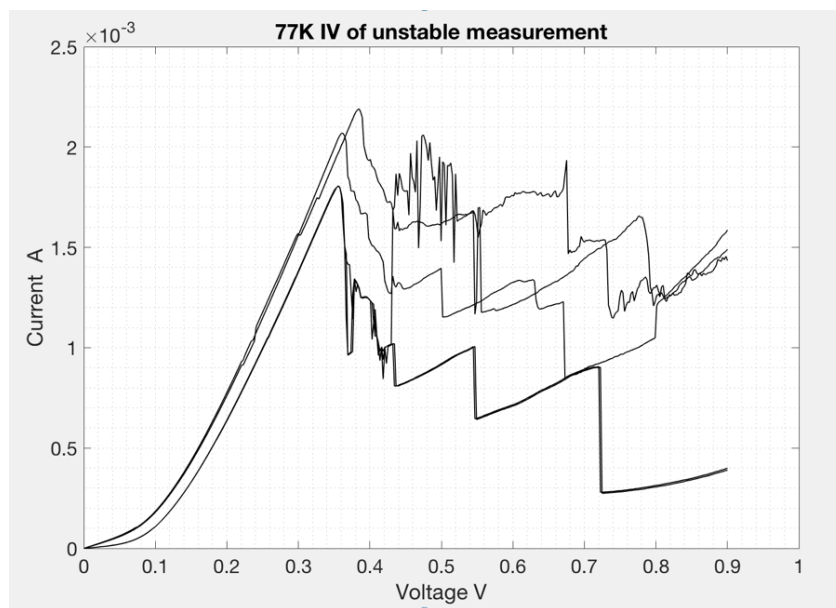


Figure 3.5: (a) IV characteristic of an RTD measured in a cryogenic probe station showing high levels of instability, potentially attributed to damaged contacts.

3.5 Micro wire bonder

Although the probe station is an efficient means of characterising our devices; the sources of error limits the reliability of our measurements. As a means of obtaining more accurate results we resorted to bonding our devices to fixed contacts on a chip holder. A micro wire bonder allows for the use of thin wire of the order of $12.5\ \mu\text{m}$ in diameter [4]. Devices connected via a microware bonder can potentially be used at frequencies beyond 100 GHz [5]. Although materials such as copper and aluminium are used, gold is often favoured due to its softness and oxidising properties. As the capillary is positioned over and lowered to the target location of the initial bond, gold wire is passed through a capillary tube where a pulse of plasma instantaneously heats, liquefies and forms a ball due to the surface tension of the gold. As the capillary is lowered, a transducer which holds the capillary transmits ultrasonic vibrations to assist in bonding the ball to the target surface (Fig 3.6). When heat is introduced the process is known as thermionic bonding. The capillary is raised in the lift off stage where the wire is continued to be fed through the capillary and is positioned over the secondary

contact pad. When conducted successfully the ball bonding method yields the most robust means of inter connecting semiconductor terminals.

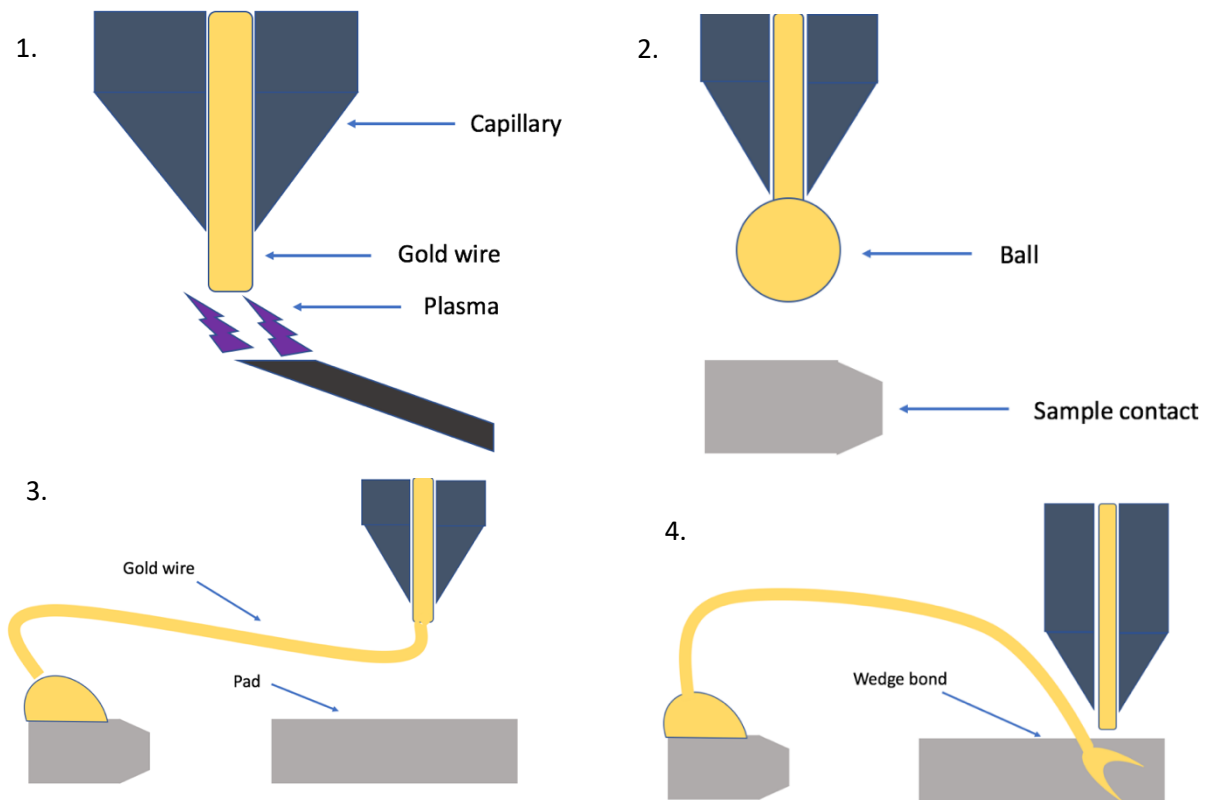


Figure 3.6: Gold ball bonding procedure. (1) Plasma rapidly heats the end of a gold wire. (2) A ball forms due to surface tension and is positioned over the initial contact. (3) The ball bonds to the contact and the capillary is positioned over the second contact to close the loop. (4) The capillary contacts the other pad and bonds a wedge, closing the loop.

However the fabrication process is time consuming and on average only 50% of all bonds are successfully bonded. In many cases during the lift off stage, the ball tears the sample's contact, exposing the InP substrate (Fig 3.8). There exists very little control over the dimensions of the ball and due to the nature of the positioning of the capillary and sample and control over the exact positioning of the ball, an issue arises due to the average diameter of the ball being approximately 2.1mm upon deposition. This allows very little room for error (approx. 0.3mm) and in many cases the ball comes into contact with contact B creating an unwanted secondary current path, rendering the device defective unless the contacted area is isolated or a probe station is used.

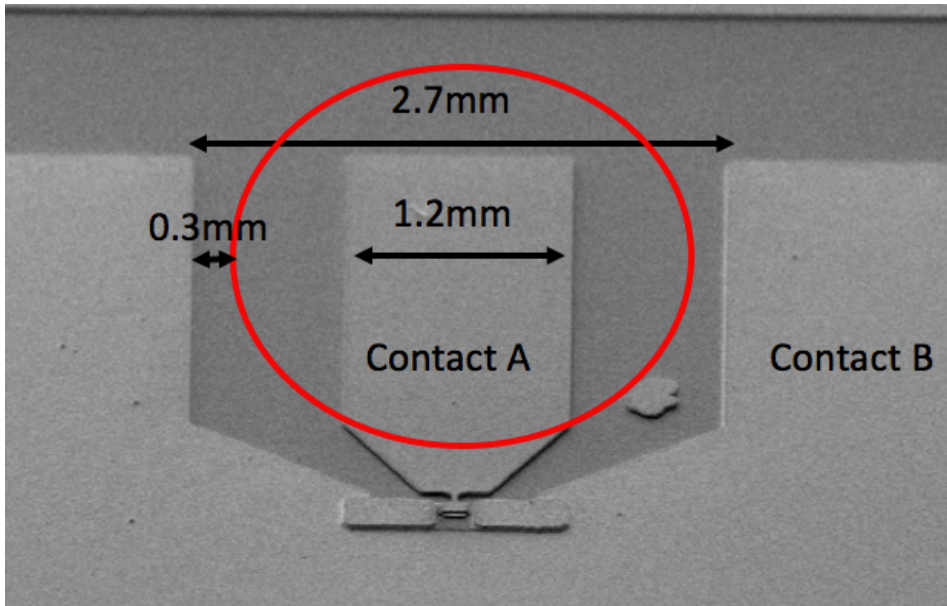


Figure 3.7: Dimensions of free space for ball bond. Ball bonds to contact A, wedge bonds to contact B. The red circle highlights the average maximum area a bonded ball can occupy, highlighting the average space available as 0.3mm.

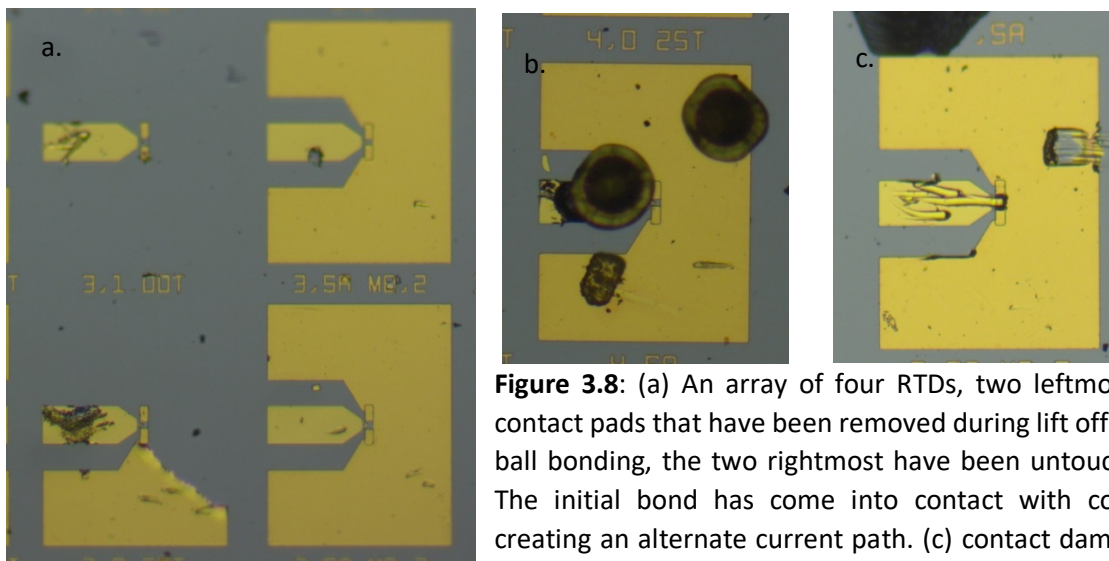


Figure 3.8: (a) An array of four RTDs, two leftmost show contact pads that have been removed during lift off stage of ball bonding, the two rightmost have been untouched. (b) The initial bond has come into contact with contact B creating an alternate current path. (c) contact damage due to tungsten probes.

3.6 Cryogenic measurements

In order to elucidate interesting features we may observe at room temperature, we comment on the interesting effects of temperature on the band structure of our RTD in chapter 2. It has been reported in the literature that at cryogenic temperatures (sub 120k) the tunnelling mechanism of certain types of heterostructures (i.e. III-Nitride tunnel diodes) becomes more prominent [6]. For this and other reasons we decided to study the RTD's characteristic under cryogenic conditions.

[3.6.1 Low temperature probe station](#)

We initially resorted to the low temperature (LT) probe station (Lakeshore PS-100) such required the use of a vacuum chamber and cryogenic storage dewar. Prior to cooling the system, the chamber was first vacuumed and reduced to a pressure of 10^{-6} bar. This process ensured that moisture upon cooling does not allow ice to form and reheating does not cause the build-up of condensation. Liquid nitrogen was stored and transported via the dewar where it was injected into the vacuum chamber. Despite a temperature range of 4.2K-475k, the lowest temperature obtained was 77k due to the boiling point of nitrogen. Modulation of the temperature was possible with a heater (Lakeland 336 Temp Controller), however our preliminary cryogenic measurements did not make use of such. We experienced the same difficulties that were faced with the room temperature probe station, namely aggravated probes. Additionally we experienced a great deal of insensitivity with the micro positioners, hence experienced difficulty in positioning our probes accurately and often damaged the contacts (Fig 3.8). We resorted to bonding our samples via the method highlighted above (3.5) to avoid such.

[3.6.2 Helium flow cryostat](#)

By bonding our samples and using a cryostat, we aimed at removing any errors found to be induced by the probe station. We resorted to an ICE Oxford dry optical cryostat that facilitates electrical measurements. The cryostat functions via a Gifford-McMahon refrigeration cycle which allow high pressure helium gas to pass into an expansion chamber where it expands and cools. A rotation valve allows the low pressure flow to cool the system and the gas returns to its original position. A caveat with using our cryostat for electrical measurements was high resistance in the internal circuitry of the system, in particular we found $175 \pm 2.5 \Omega$ due to 42-SWG constantan twisted pair wires. We resorted to a four terminal measurement (4 pt sensing) as a means of directly characterising our device (Fig 3.9). We connect two extra terminals across our RTD that will measure the potential difference across, acting as a voltmeter with miniscule current flowing through, hence we observe very little voltage drop. By Kirchhoff's law we are able to evaluate the current at every junction to be constant, we then measure the voltage across our RTD (V_m) and the current measured (I_m).

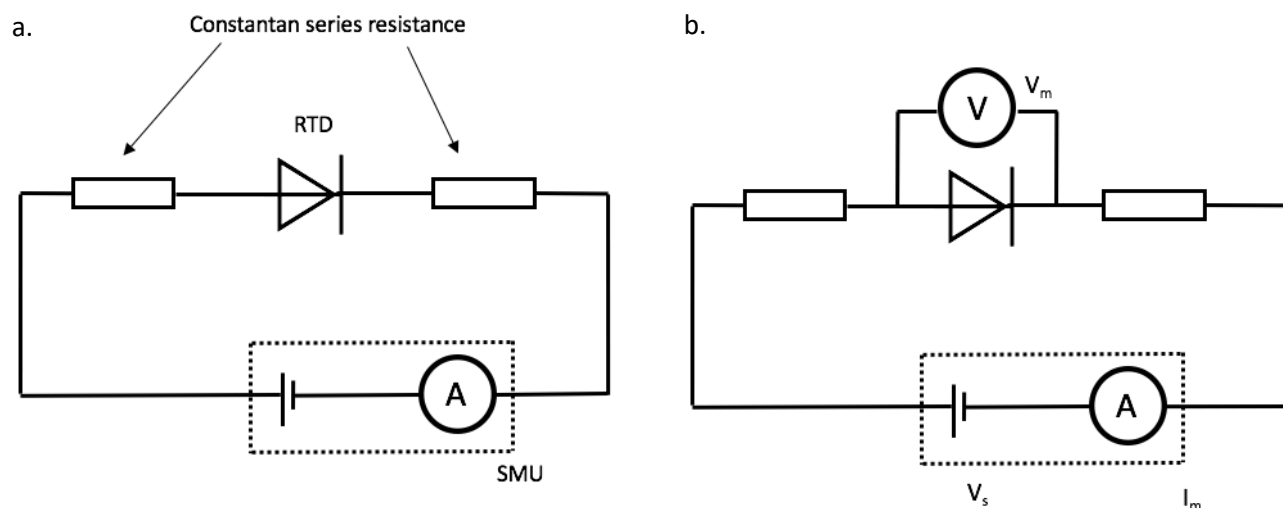


Figure 3.9: (a) 2 point measurement with large in series resistance due to constantan wiring of the cryostat, the SMU is highlighted as a cell and ammeter sourcing voltage and measuring current. (b) Standard 4-point measurement, two terminals measuring the potential difference across our RTD (V_m), and two sourcing voltage (v_s), measuring current (I_m).

We've outline a range of methods that we employed in our study. They range from methods of characterisation to modification and we have briefly commented on the difficulties and sources of error in our methods. We note the difficulty faced when studying our sample under cryogenic conditions and when preparing our RTDs with the micro wire bonder as well as how effective apparatus such as the SMU/probe station were. In the forthcoming chapter we pay close attention to our results and assess how effective our methods were.

Bibliography

- [1] A. R. Clarke, *Microscopy techniques for materials science.*, CRC Press (electronic resource), 2002.
- [2] e. a. J.R. Krogmeier, Focused ion beam modification of atomic force microscopy tips for near-field scanning optical microscopy, vol. 79, *Appl. Phys. Lett.*, 2001.
- [3] J. Melngailis, Focused, ion beam lithography, vol. B80/81, *Nuclear Instr. and Meth. in Phys. Res.*, 2993, p. 1271.
- [4] A. e. c. a. packaging., ""Gold Bonding Wire and Ribbon: Wire for Automatic Bonders",” 2014. [Online]. Available: <http://www.ametek-ecp.com/products/componentswire/wireandribbon/goldwireandribbon>. [Accessed 2017].
- [5] V. V. e. al., “Design and experimental evaluation of compensated bondwire interconnects above 100 GHz,” *International journal of Microwave and Wireless Technologies.* , vol. 7, no. 3-4, pp. 261-270, 2015.
- [6] D. L. e. al., “Temperature-dependence of negative differential resistance in GaN/AlGaN resonant tunneling structures,” *Semiconductor Science and Technology*, vol. 28, 2013.

Chapter 4- Experimental Results

4.1 Introduction

In the previous chapter we have described the methods used to obtain our results. We now present in this chapter the combination of the methods introduced in chapter 3 with the hypothesis established in chapter 2 to increase the bit density of the QCPUF such that our UO (unique object) has an increased level of complexity. We used a FIB (focused ion beam) to introduce multiple areas of confinement (by laterally restricting areas) within the heterostructure. We present our results through the characterisation of our RTDs in different conditions and observed a number of features that are of interest. Our results bare close resemblance to the results of previous work carried out by Reed et al. We compare and contrast such results however as a solution to the bit density problem of the QCPUF further investigation is required.

4.2 Increased Bit Density

4.2.1 Introduction

In the area of forensics the familiar fingerprint which is used in identification relies on the complex structure and random pattern of its own minutia. There exist over eight different types of minutia that range from the small ridges and islands to the complex bifurcations on one's fingerprint. In a nutshell, an algorithm converts the unique pattern derived from the combination of different minutia to generate a unique identity that is then the basis for identification and security.

Previous work on QCPUF's using RTDs only rely on the peak position as the only minutia and hence source of true uniqueness. To realise the full potential of a 'quantum fingerprint'; the need to incorporate further minutia will undoubtedly bring the QCPUF closer to a fingerprint like architecture. It has been proposed in the literature [1] that in addition to the peak position one can utilise the valley, peak to valley ratio (PVR) and tunnelling region to use as the UO.

We explored up to 8 different etch designs over 69 devices however our most recurring results were characterised as: 1) second resonance peak and 2) bumps within NDR region. Prior to modifying our devices with the FIB, we recorded the IV characteristic in the negative bias (axis inverted), however at times we observed interesting features in both biases, as a comparison metric we were only able to compare our before and after sweeps in the negative bias. In many cases we present only the IV characteristic under the negative bias, as generally broader peaks and larger PVR are observed under such bias. We also produced a set of devices whose final surface area was less than $4 \mu\text{m}^2$ (the current minimum of such RTDs) with a clear NDR region resulting in an increase in bit density per unit volume.

We will begin by presenting the different designs for each etch type presenting the data, in many cases the designs yielded non-functioning devices. Only a select few of the etch designs produced devices that were functioning post FIB and even fewer devices gave interesting results on the IV characteristic that were worth investigating.

4.2.2 Etch designs and parameters

We began with 195 devices on our chip, 133 of these devices were functioning and were considered suitable for modification by the FIB. We modified 69 with the FIB and out of these approximately 30 were functioning post modification. Overall we proposed eight etch designs in an attempt to successfully introduce more confined states. We observed that some designs were more successful than others and the overview of the designs can be summarised in Table 4.1 below.

However it is important to note that in these measurements we did not consider parameters that would affect etch rate from the FIB; i.e. the intensity of the Gallium ion beam, etc. such are discussed further in chapter 5.

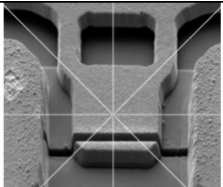
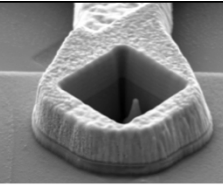
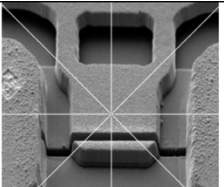
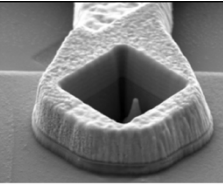
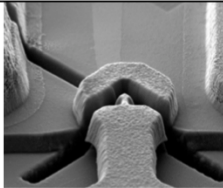
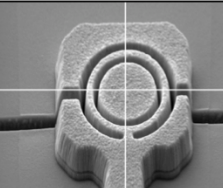
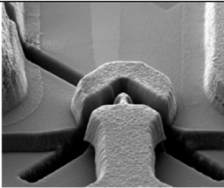
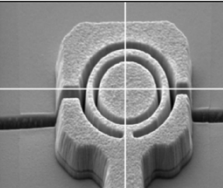
 <p>Lateral 20 etched 6 functioning post FIB 30% success rate</p>	 <p>Diamond 5 etched 3 functioning post FIB 60% success rate</p>	 <p>Lateral 20 etched 6 functioning post FIB 30% success rate</p>	 <p>Diamond 5 etched 3 functioning post FIB 60% success rate</p>
 <p>Arrow 5 etched 0 functioning post FIB 0% success rate</p>	 <p>Ring + rectangle 4 etched 4 functioning post FIB 100% success rate</p>	 <p>Arrow 5 etched 0 functioning post FIB 0% success rate</p>	 <p>Ring + rectangle 4 etched 4 functioning post FIB 100% success rate</p>

Table 4.1: SEM images of etched RTDs showing an overview and summary of the etch designs and their success rate. Each design was repeated a number of times and obtained various success rates which we attribute to our control of the FIB. Each etch design varied slightly in FIB parameters and dimensions.

4.2.3 Lateral etch

We began our investigation with lateral etches gradually decreasing the area of the device such that we aim to identify the cross-over from 2D to 1D confinement. Our goal was to explore the potential of confining our electrons to a further two dimensions such that we create a 1D structure (quantum wire). Unfortunately, the majority of our results were unsuccessful in showing clear signs of increased confinement and many of which were defective post FIB. However some modified devices did yield interesting results. It is important to note that some lateral etches were solely for testing preliminary FIB parameters and resulted in significantly damaged devices. Devices whose IV characteristic did not present a clear NDR, were characterised as defective devices and exhibited high instabilities, high in parallel/in series resistance and at times showed open/short circuits. Our devices' initial surface area ranged from $4 \mu\text{m}^2$ to $25 \mu\text{m}^2$ sized mesas. We explored a wide variety of dimensions that ranged from reducing our structure by a factor of two to a factor of four (Fig 4.1). Overall our device areas ranged from $2 \mu\text{m}^2$ to $13 \mu\text{m}^2$.

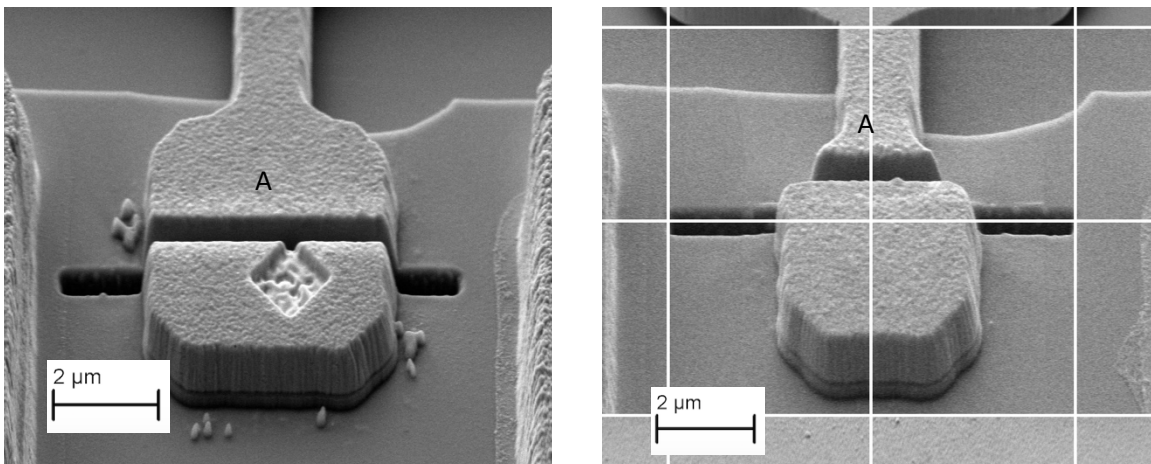


Figure 4.1: SEM image of device B4 (left) showing a lateral etch that has thus reduced the active area by half. A9 (right) post FIB RTD, with a minimal active region marked by A.

Out of the nineteen devices modified, six were functioning post-FIB (Table 4.2). We attribute such a low success rate to the intensity of the Ga ion beam which can affect the doping profile of the layers, however as we etched more structures we altered the intensity of the beam and milling duration to aggravate the active regions much less.

A primary feature we observed with all functioning devices post FIB was a decrease in both current and voltage resonance value. We attribute this to the reduced size of the device and to the proportionality of current density. Where the current density (J) is a measure of the electric current (I) per unit area of cross section (A); $J=I/A$, assuming that the motion of current is orthogonal to the surface A .

We observe multiple interesting factors post FIB for device B7 (Fig 4.2). Dissecting our IV characteristic into distinctive regions; beginning with the tunnelling region. By mere observation we can see a decreased stability in the tunnelling region which may be attributed to defects induced by the FIB, an undesirable feature we wish to avoid. We observe a decreased resonance peak current and observe a secondary peak at 0.48V.

Device	Area i μm^2	initial resonance peak	initial resonance valley	PVRi	final resonance peak	final resonance valley	PVRf	Area f μm^2	Area reduction
A3	25	(0.4V, 7.10mA)	(0.76V, 0.90mA)	7.90	(0.47V, 10.40mA)	(0.62V, 7.90mA)	1.30	13.00	1.90
A9	9	(0.36V, 2.60mA)	(0.68V, 0.35mA)	7.43	(0.37V, 1.80mA)	(0.51V, 1.20mA)	1.50	2.25	4.00
B4	16	(0.36V, 5.70mA)	(0.72, 0.75mA)	7.60	(0.36, 2.90mA)	(0.58, 1.20mA)	2.40	8.00	2.00
B7	9	(0.35, 3.30mA)	(0.71, 0.45mA)	7.30	(0.37, 1.20mA)	(0.51, 0.90mA)	1.30	3.00	3.00
C4	16	(0.36, 5.20mA)	(0.73, 0.67mA)	7.80	(0.38, 3.0mA)	(0.52, 2.20mA)	1.36	5.60	2.80
D4	16	(0.37, 5.10mA)	(0.73, 0.65mA)	7.80	(0.38, 4.50mA)	(0.48, 3.90mA)	1.15	6.00	2.60

Table 4.2: Devices etched laterally, showing their initial and final peak and valley positions and their corresponding initial (PVR_i) and final (PVR_f) peak to valley ratio. In all cases we observe a decrease in PVR (as low as 1.15).

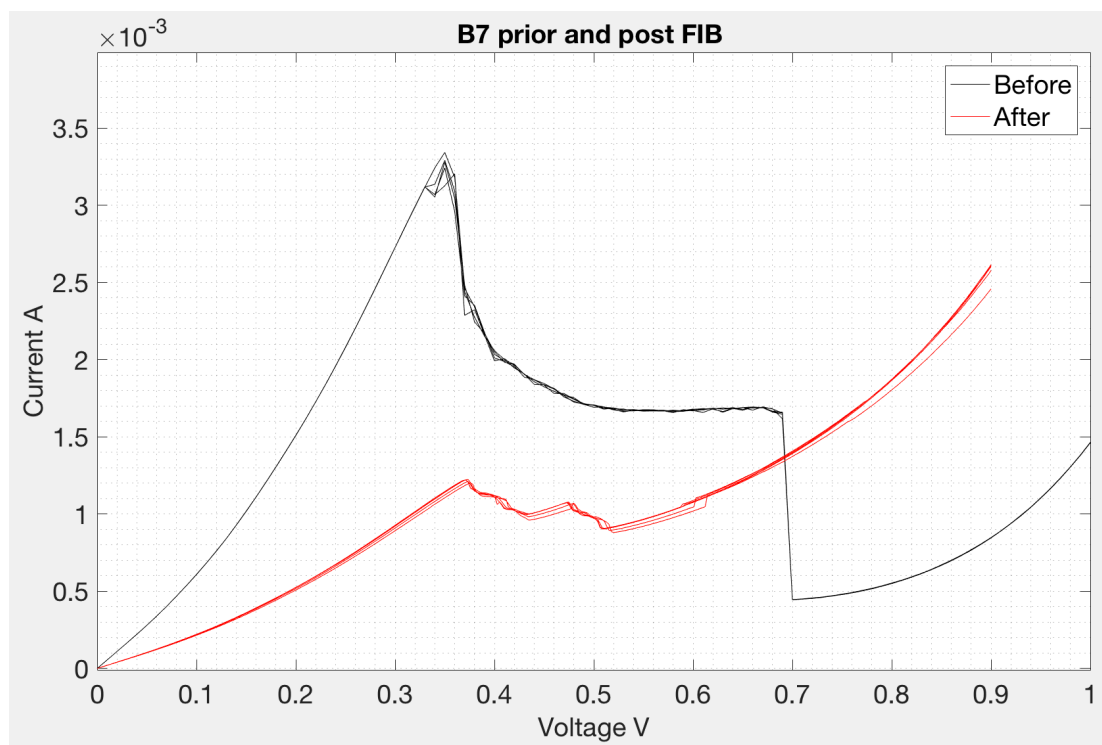


Figure 4.2: IV characteristic of device B7 before and after treatment with FIB, where a visible secondary peak and corresponding NDR is visible post modification (red). Minimal in series and in parallel resistance is observed.

In other cases, some devices exhibited instabilities displayed through the manifestation of in parallel resistance. This may be attributed to the measurements apparatus, namely the probe contacts. We observe an increase in resonance current in three out of our five repeated measurements. We observe a similar post FIB IV characteristic with device A9, this device exhibited the smallest surface area of a

working device ($2.25 \mu\text{m}^2$) operating at 25% lower power. As A9 was our smallest functioning device we have ultimately increased the bit density by a factor of 4.2 (Fig 4.3).

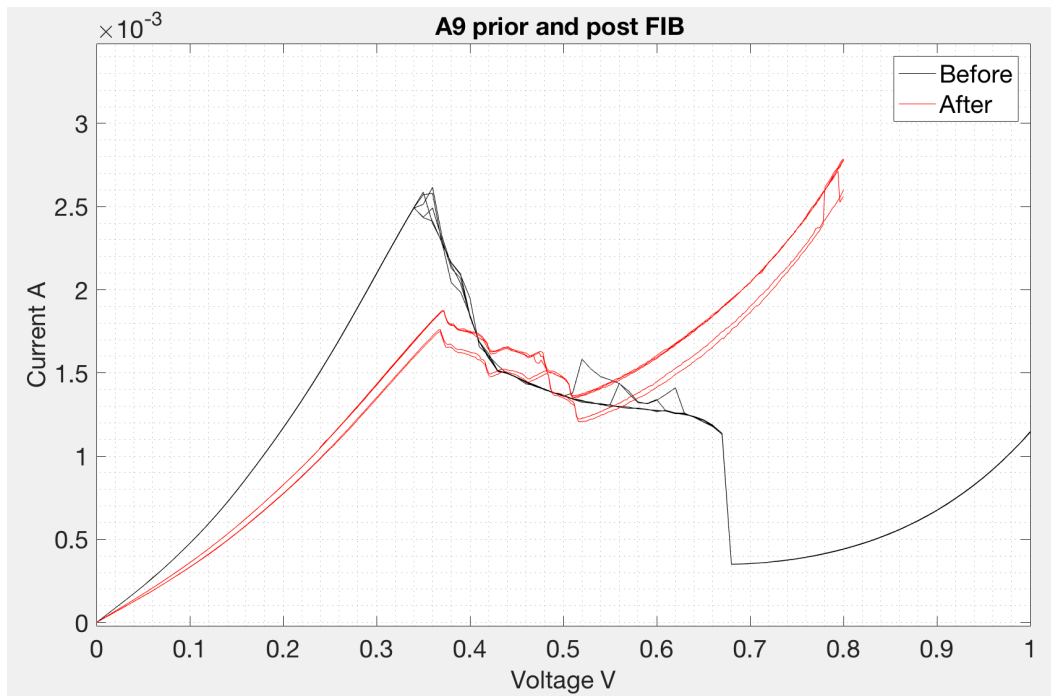


Figure 4.3: IV characteristic of A9 before and after being treated with a FIB showing instability in the NDR and increase in parallel resistance causing a shift in peak current. The before IV characteristic shows a more defined resonance peak and stable PDR.

4.2.4-Diamond etch

Following our improved etch parameters we employed a design that yielded a 60% success rate. The aim of the diamond etch was to induce maximum probability of confinement within the corners of the cavity (Fig 4.4). Our devices' initial surface area ranged from $4 \mu\text{m}^2$ to $36 \mu\text{m}^2$ sized mesas, with a maximum confinement post FIB of up to 55nm (Table 4.3).

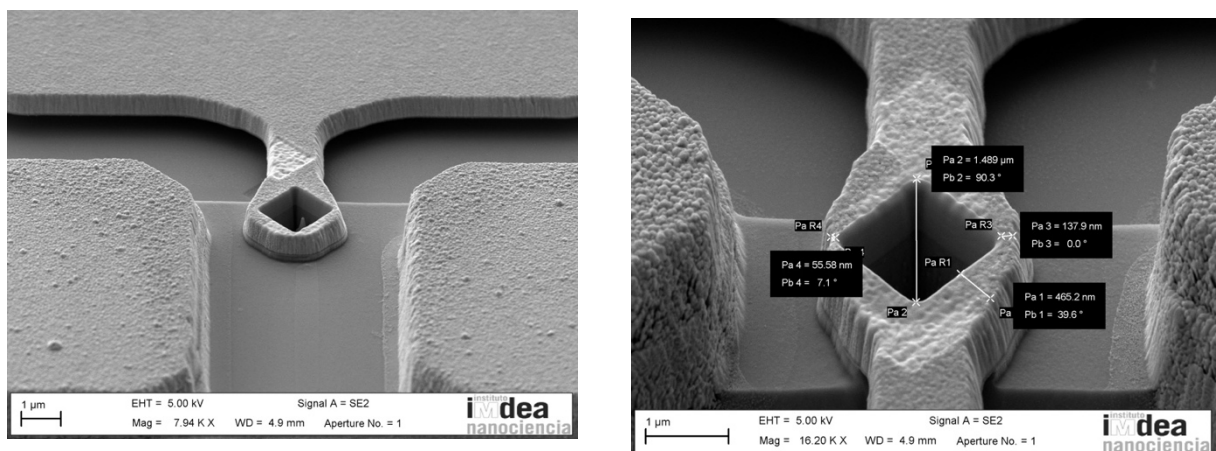


Figure 4.4: SEM images of A11 post FIB (left) with a cavity surface area of $1.25 \mu\text{m}^2$, D11 (right) with a cavity surface area of $1.50 \mu\text{m}^2$. Both FIB etches were identical in dimension and etch rate.

Chip no#	Device	Area i μm^2	initial resonance peak	initial resonance valley	PVRi	final resonance peak	final resonance valley	PVRf	Area f μm^2	Area reduction
2	E1	36	(0.42V, 10.50mA)	(0.73V, 1.20mA)	8.75	(0.93V, 6.70mA)	(0.92V, 4.40mA)	1.52	13.00	2.77
1	D11	4	(0.34V, 1.50mA)	(0.68V, 0.18mA)	8.33	(0.36V, 1.50mA)	(0.49V, 1.20mA)	1.25	2.50	1.60
1	A11	4	(0.34V, 1.30mA)	(0.68V, 0.17mA)	7.65	(0.36V, 1.30mA)	(0.50V, 1.0mA)	1.30	2.75	1.45

Table 4.3: Devices etched with a diamond cavity, showing their initial and final (post FIB) peak and valley positions and their corresponding peak to valley ratio (PVR). We observe two devices with final surfaces areas of less than $4 \mu\text{m}^2$.

Out of the three functioning devices (E1, D11, A11) we observed two devices (D11 & A11) in particular that not only gave relatively stable and repeatable IV characteristics but also a hint of secondary resonance peak. The third device (E1); although functioning exhibited high instabilities, we were unable to observe a consistent and repeatable resonance peak, although we are able to extract an average peak and valley position, we characterise such a device as unstable (Fig 4.5).

What is interesting to note with D11 and A11 is the existence of a second resonance peak post modification. There exists in both cases after the resonance peak and for both devices of identical size prior modification and near identical post modification sizes, the second peak exists at similar locations with an offset of ($\pm 0.01\text{V}$, $\pm 0.002\text{mA}$). A phenomena we initially attributed to increased confinement.

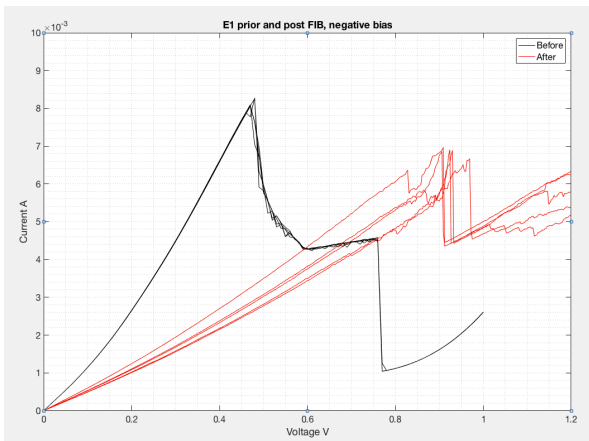
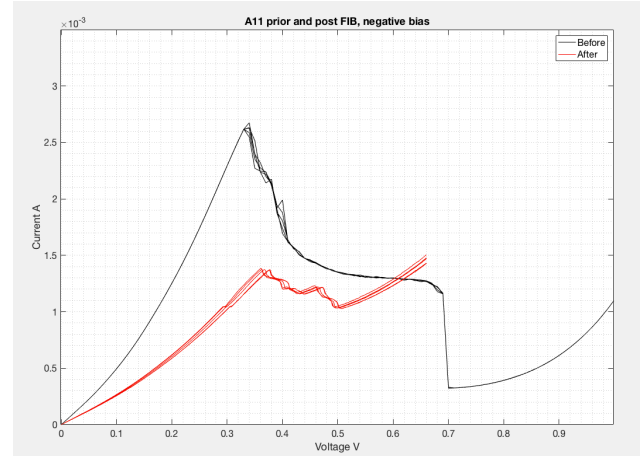
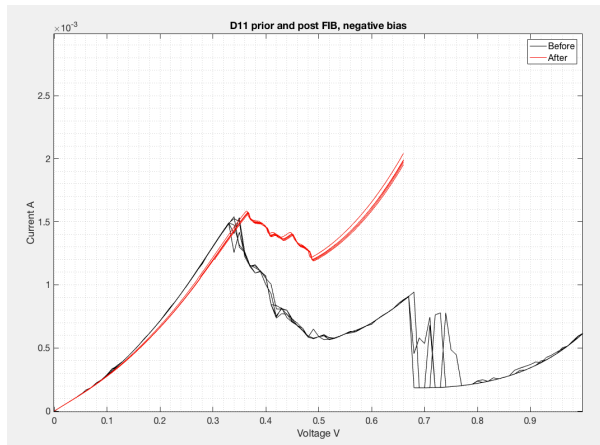


Figure 4.5: IV characteristic of the functioning diamond etch design. Top left- D11 showing a double peak and high in parallel resistance, top right- A11 showing a double PDR with significantly less in parallel resistance. E1 (bottom left) shows an unstable device with both high in parallel and in series resistance. An observable NDR yet poorly defined peak and valley exists.

4.2.4 Arrow etch

We then aimed to create a structure with as much confinement as possible, for this we aimed for etches that produced a minimum active region.

However upon post FIB characterisation, we report that none of our devices were functioning. We attribute such to the fact that our etch parameters did not fully consider the structure of the device. We believed that we etched in such a way that limited the current flowing through the device, in many cases we removed parts of the device resulting in no current being able to flow at all. This is because the trench milled by the FIB into the InP substrate, completely isolating the active region from the bottom contact such causes the formation of an open circuit (Fig 4.6).

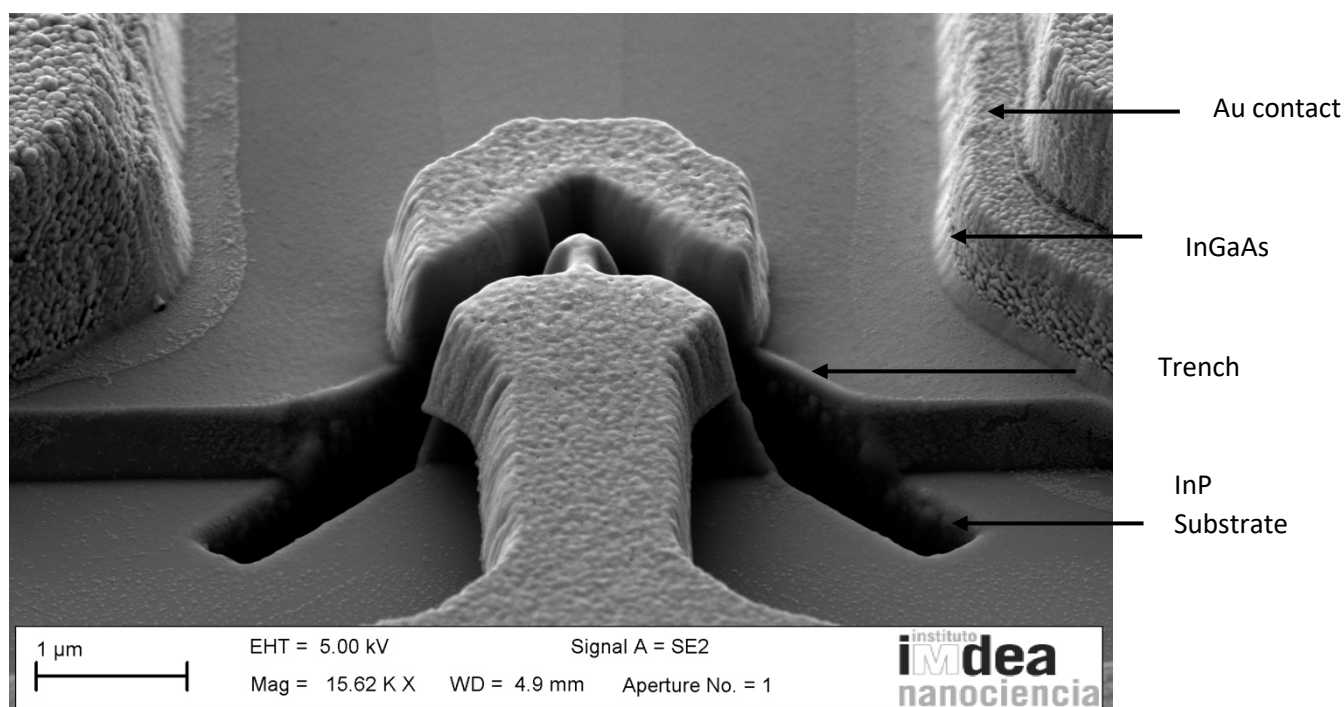


Figure 4.6: SEM image of a typical arrow etch design showing the trenches within the InGaAs that isolate the active region and hence causing an open circuit. The active region consists of both the arrow structure and the irregular shape below

4.2.5 Ring+Rectangle etch

The next design features a ring with irregular rectangular active regions below the ring, and part of the air bridge also contributing as an active region. This particular design had a 100% success rate. Initially we aimed for the active region to just be the ring, however due to limitations in our method of applying the FIB, we were unable to fully isolate the ring (Fig 4.7). The rectangular offset as a result was irregular in dimensions. Again we observe a decreased PVR however our values of current density do not show proportionality. This may be due to miscalculated areas with regards to the active region and possibly due to a build-up of a large in parallel resistance. The smallest PVR (1) of any device was observed with device B7 (Table 4.4).

Device	Area i μm^2	initial resonance peak	initial resonance valley	PVRi	final resonance peak	final resonance valley	PVRf	Area f μm^2	Area reduction
A7	16	(0.37V, 6.0mA)	(0.72V, 0.8mA)	7.50	(0.45V, 5.8mA)	(0.63V, 1.9mA)	3.05	4.01	3.99
B7	16	(0.35V, 5.3mA)	(0.72V, 0.7mA)	7.57	(0.40V, 5.8mA)	(0.53V, 3.9mA)	1.00	2.39	1.67
C7	16	(0.35V, 4.9mA)	(0.73V, 0.6mA)	8.20	(0.42V, 8.9mA)	(0.48V, 5.8mA)	1.53	3.41	1.17
D7	16	(0.36V, 5.9mA)	(0.73V, 0.61mA)	9.67	(0.42V, 8.8mA)	(0.50V, 7.1mA)	1.24	3.86	1.04

Table 4.4: Devices etched with the ring + rectangle design, showing their initial and final (post FIB) peak and valley positions and their corresponding peak to valley ratio (PVR). Devices B7, C7 and D7 all had final areas below $4 \mu\text{m}^2$.

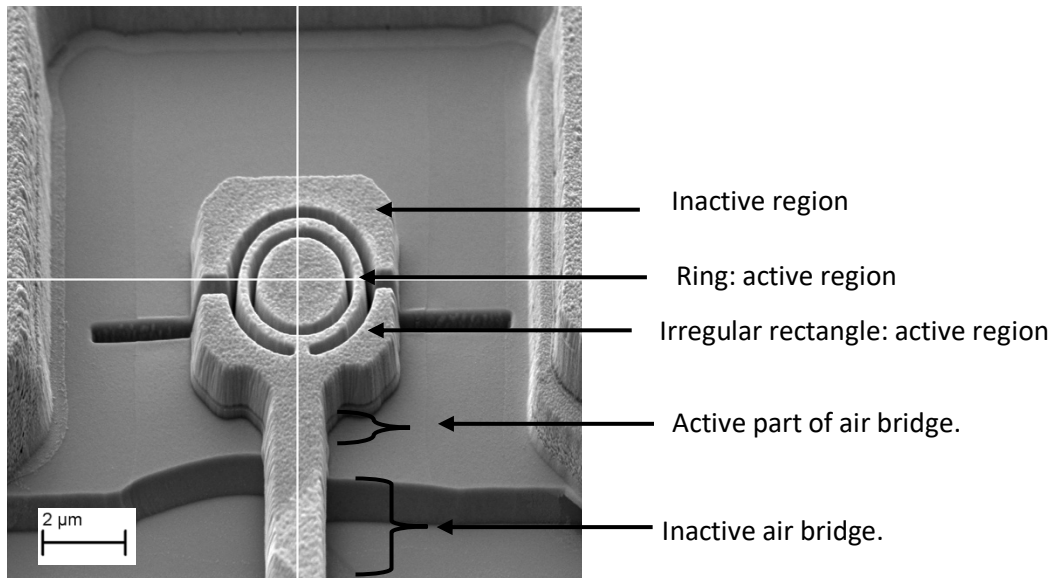


Fig 4.7: SEM image of device A7, highlighting the active and inactive regions of the ring and irregular rectangle, in addition to the irregular rectangle, part of the air bridge appears to be active, in our calculations of area we neglect such.

Although all devices were still functioning, not all exhibited good stability. Devices A7 and B7 showed clear signs of a repeatable peak and valley. Devices C7 and D7 (Fig 4.8) were extremely unstable and a consistent peak and valley were difficult to locate thus an average/approximation had to be evaluated. However this etch exhibited a hint of an artefact with one device (A7), namely small bumps within the NDR region (Fig 4.9). This was the first instance of bumps in the NDR that may be due to resonant tunnelling in other dimensions as previously seen by [2].

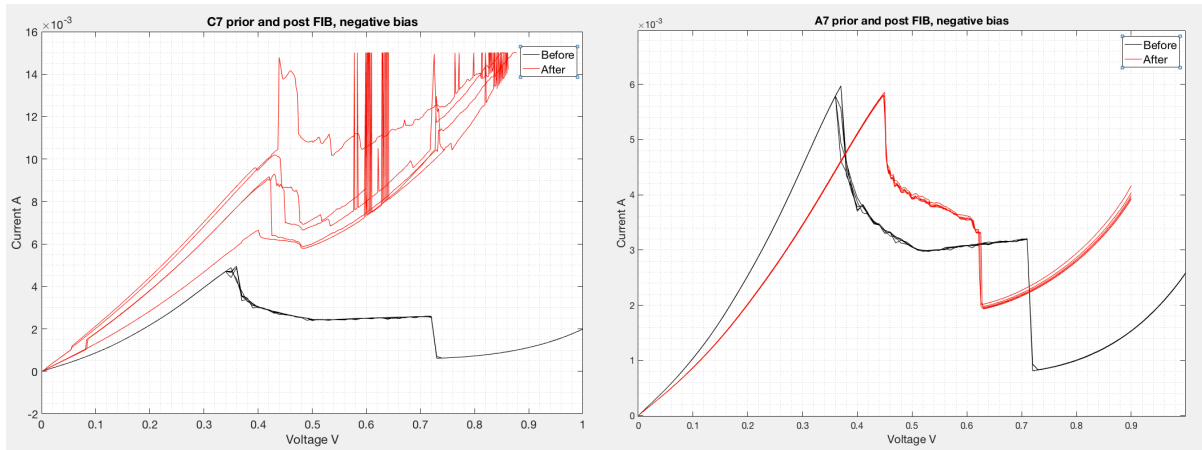


Figure 4.8: Devices C7-showing an unstable IV characteristic with varying peak and valley values. A7-stable IV characteristic with large in parallel and slight in series resistance in addition to a reduced PVR and bumps in NDR.

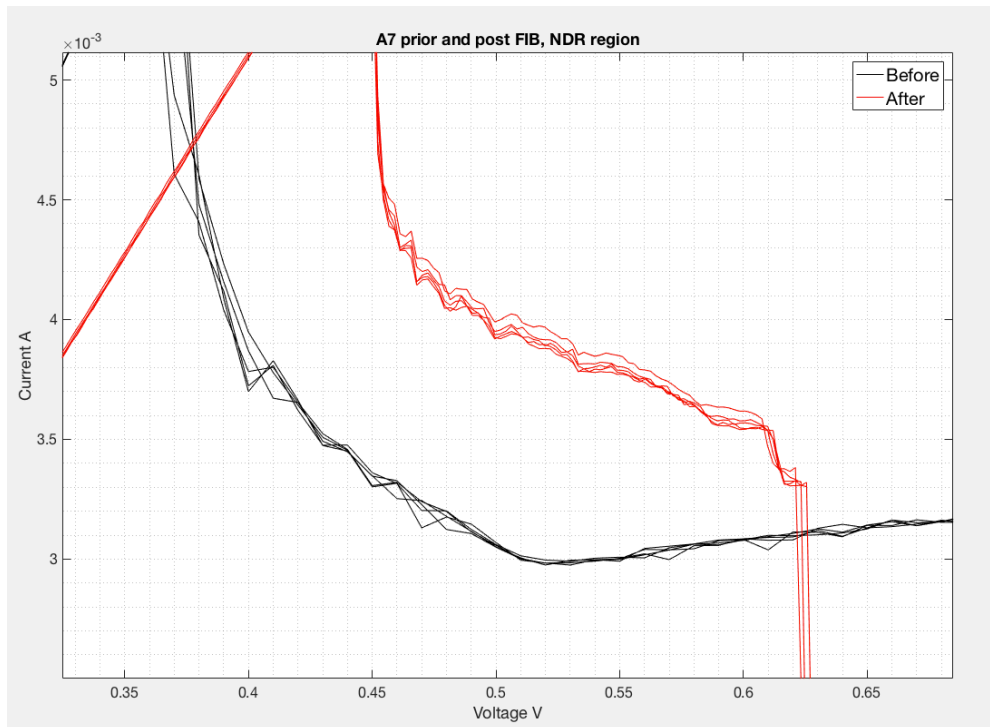


Figure 4.9: Close up of bumps in NDR region of device A7 before and after modification with FIB. Small artefacts within the 'after' sweep are found in voltage range 0.45-0.55 V

4.2.6 Ring+Triangle Etch

It was highlighted that in the previous design that the irregular rectangular below the ring was deemed an active region. In the current design we aimed at minimising the surface area however due to the difficulties in ion beam positioning we could only manage to etch below the ring to only a triangle. The resulting design was a ring + triangle (Fig 4.10), this particular design yielded a 100% success rate (Table 4.5).

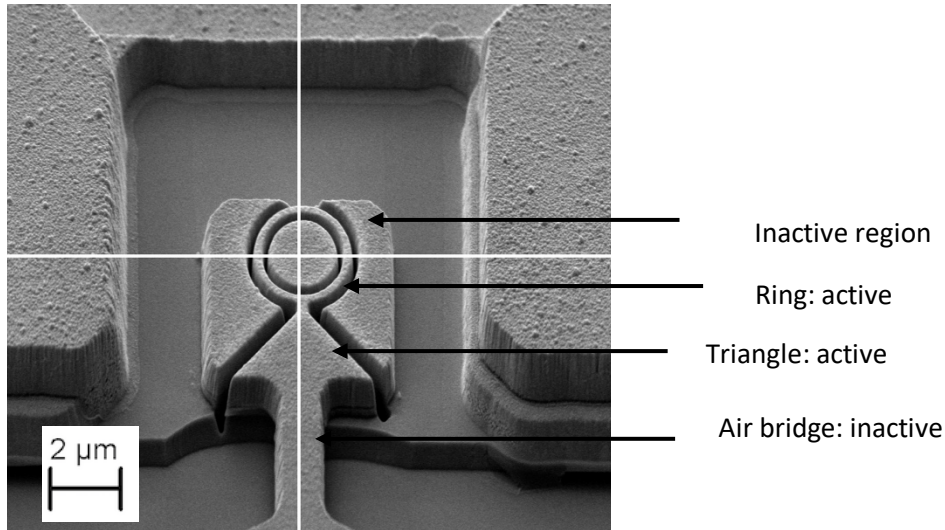


Figure 4.10: SEM image of typical ring + triangle design, device-B4 after being etched. The active regions of the ring and the triangle are highlighted.

Device	Area, μm^2	initial resonance peak	initial resonance valley	PVRi	final resonance peak	final resonance valley	PVRf	Area, μm^2	Area reduction
A4	25	(0.39V, 8.8mA)	(0.73V, 1.2mA)	7.33	(0.44V, 4.5mA)	(0.55V, 3.9mA)	1.15	3.56	7.02
B4	25	(0.38V, 8.1mA)	(0.74V, 1.2mA)	6.75	(0.38V, 4.8mA)	(0.51V, 1.8mA)	2.67	5.95	4.20
C4	25	(0.37V, 7.5mA)	(0.74V, 0.93mA)	8.06	(0.47V, 1.9mA)	(0.48V, 1.0mA)	1.90	4.06	6.16

Table 4.5: Devices etched with the ring + rectangle design, showing their initial and final (post FIB) peak and valley positions; and their corresponding peak to valley ratio (PVR).

This particular etch design produced the most interesting results. Device A4 featured two small bumps in the NDR that we did not observe prior to modification. However our most prominent instance of a double peak was found with device B4. In this device we observed an obvious secondary peak, while under the positive bias we observed a bump in the tunnelling region. Interestingly with device B4 (Fig 4.11), the secondary peak in both bias have very similar voltage ratios ($\pm 0.02\text{V}$). Such may be attributed to tunnelling through a secondary confined level, or due to a secondary RTD created in series.

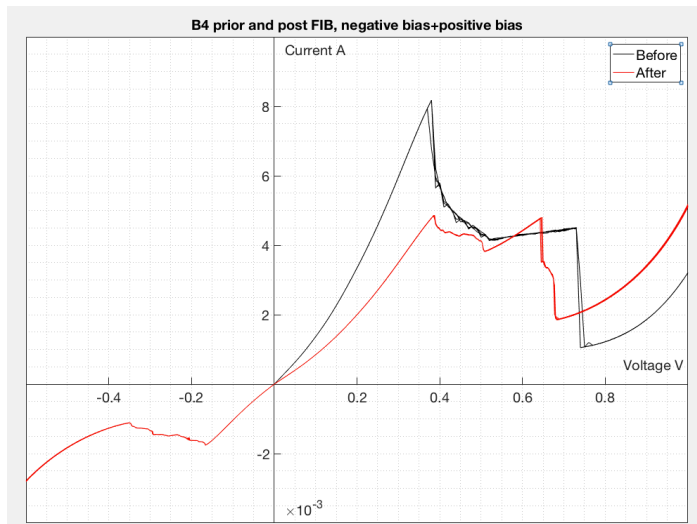


Figure 4.11: IV characteristic showing a distinctive double resonance peak in the negative bias and a slight bump in the positive bias of the post FIB curve. Primary resonance peak at (0.38V, 4.8mA) and secondary peak at (0.64V, 4.7mA). Additionally minimal in parallel and in series resistance is observed.

Device C4 initially exhibited the same artefact in the negative bias, however the double peak was unstable and as a result we were unable to record evidence of such, rather what was recorded in the negative bias were the small bumps (up to three) in the NDR we have previously observed (Fig 4.12). Furthermore, we observed a plateau in the positive bias (negative region of graph) in addition to a peak and valley. The plateau existed in approximately the same region as the resonance peak would have been expected to be. The resonance peak in the negative bias exhibited a voltage shift due to in series resistance.

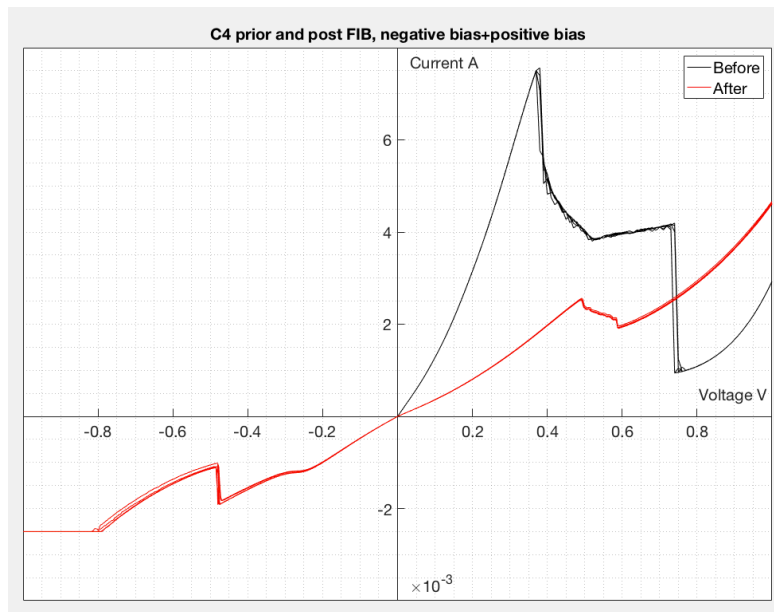


Figure 4.12: IV characteristic of device C4, a post PVR of 1.9 is observed and slight in series resistance in the negative bias. The positive bias shows a plateau at (-0.23V, -1.25mA) in the positive (negative region of graph) bias.

4.2.7 Hole Etch

As the issue of FIB-sample alignment rendered many of our devices unpredictable, we explored the possibility of creating multiples areas of confinement on the same device by proposing a design that consists of many small holes etched periodically across the device. The number of holes on each device ranged from 60-85 depending on the FIB-sample alignment. We increased the milling duration and lowered the beam intensity in the hopes that we would aggravate the active regions as little as possible. Both each hole diameter and the inter hole spacing measured an average of 0.2 μm (Fig 4.13).

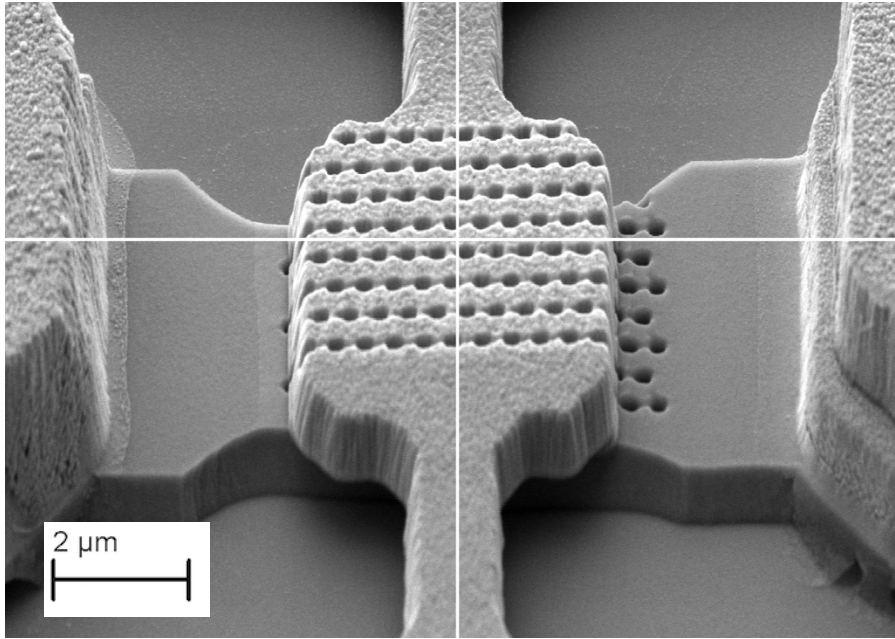


Figure 4.13: SEM image of Device G9 with an array of approximately 84 holes milled, each hole of diameter 0.2 μm approx., FIB misalignment shows holes being etched onto InP substrate.

Such a design provided us with a 66% success rate (Table 4.6), however where we would usually expect the difference in averages of final to initial PVR to be large ($\sim 5 \pm 1.0$); it appears that by milling holes into our structure it resulted in a final average PVR of the same order of magnitude 0 ± 0.99 (Table 4.6).

Device	Area i μm^2	initial resonance peak	initial resonance valley	PVRi	final resonance peak	final resonance valley	PVRf	Area f μm^2	Area reduction
G9	16	(0.37V, 3.87mA)	(0.72V, 0.49mA)	7.89	(0.42V, 5.5mA)	(0.74V, 0.71mA)	7.75	15.17	1.05
H9	16	(0.39V, 7.11mA)	(0.75V, 0.84mA)	8.46	(0.41V, 5.0mA)	(0.74V, 0.61mA)	8.20	15.00	1.07
I9	16	(0.39V, 7.83mA)	(0.76V, 0.94mA)	8.33	(0.36V, 4.8mA)	(0.72V, 0.58mA)	8.28	15.90	1.01
A10	9	(0.35V, 3.70mA)	(0.71V, 0.50mA)	7.40	(0.40V, 2.1mA)	(0.54V, 1.40mA)	1.50	3.66	2.46

Table 4.6: Devices etched with the holes design, showing their initial and final (post FIB) peak and valley positions; and their corresponding peak to valley ratio (PVR).

For all functioning devices we observed the same relic previously seen, namely bumps in the NDR. In some cases they were more prominent than others, this was particularly true with device A10 (Fig 4.14); prior to milling holes we milled a square cavity of an area of 4.75 μm^2 . In this case we reduced the area of the active region below the minimum standard as a result of the combination of etches. This particular device showed a device with bumps again within the NDR.

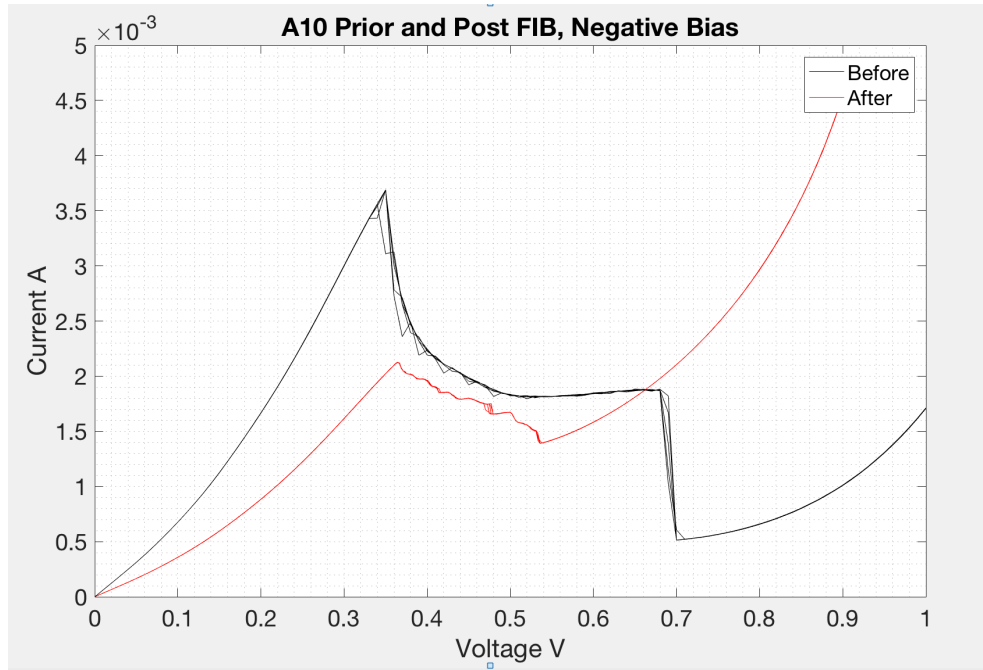


Figure 4.14: IV characteristic of device A10, The NDR showing subtle bumps that were not observed in the before sweep. We observe minimal in series and parallel resistance and a decrease in PVR characteristic of devices post FIB.

4.2.8 Square etch

A number of interesting results were found as a result of the diamond etch explored previously, in an attempt to investigate such further we repeated the stencil used however rotating such by 45°. The resulting design was a square cavity that exhibited a 63% success rate. On average we reduced the area by a factor of two (Table 4.7).

Device	Area i μm^2	initial resonance peak	initial resonance valley	PVRi	final resonance peak	final resonance valley	PVRf	Area f μm^2	Area reduction
B10	9	(0.35V, 3.12mA)	(0.69V, 0.41mA)	7.61	(0.36V, 2.20mA)	(0.53V, 1.40mA)	1.57	5.76	1.56
C10	9	(0.34V, 2.80mA)	(0.70V, 0.35mA)	8.00	(0.55V, 1.67mA)	(0.65V, 0.87mA)	1.91	n/a	n/a
D10	9	(0.34V, 1.53mA)	(0.67V, 0.18mA)	8.50	x	x	x	n/a	n/a
F10	9	(0.36V, 3.50mA)	(0.69V, 0.52mA)	6.73	(0.36V, 3.0mA)	(0.51V, 2.1mA)	1.42	5.00	1.80
E10	9	(0.34V, 2.62mA)	(0.69V, 0.36mA)	7.27	x	x	x	3.30	2.72
G1	36	(0.45V, 11.7mA)	(0.72V, 1.47mA)	8.24	(0.37V, 5.8mA)	(0.58V, 2.6mA)	2.23	15.36	2.34
G10	9	(0.34V, 3.40mA)	(0.70V, 0.45mA)	7.55	(0.36V, 2.8mA)	(0.51V, 1.9mA)	1.47	3.71	2.42
H10	9	(0.34V, 2.80mA)	(0.69V, 0.35mA)	8.00	x	x	x	5.00	1.80

Table 4.7: Devices etched with the holes design, showing their initial and final (post FIB) peak and valley positions; and their corresponding peak to valley ratio (PVR).

Despite keeping our etch parameters unchanged, with every functioning device post FIB we observed the same feature in the NDR region; bumps. However three devices in particular exhibited the most prominent of all bumps that appeared to have grouped near the resonance peak and valley, such were observed with devices F10 (Fig 4.15), G1 and G10.

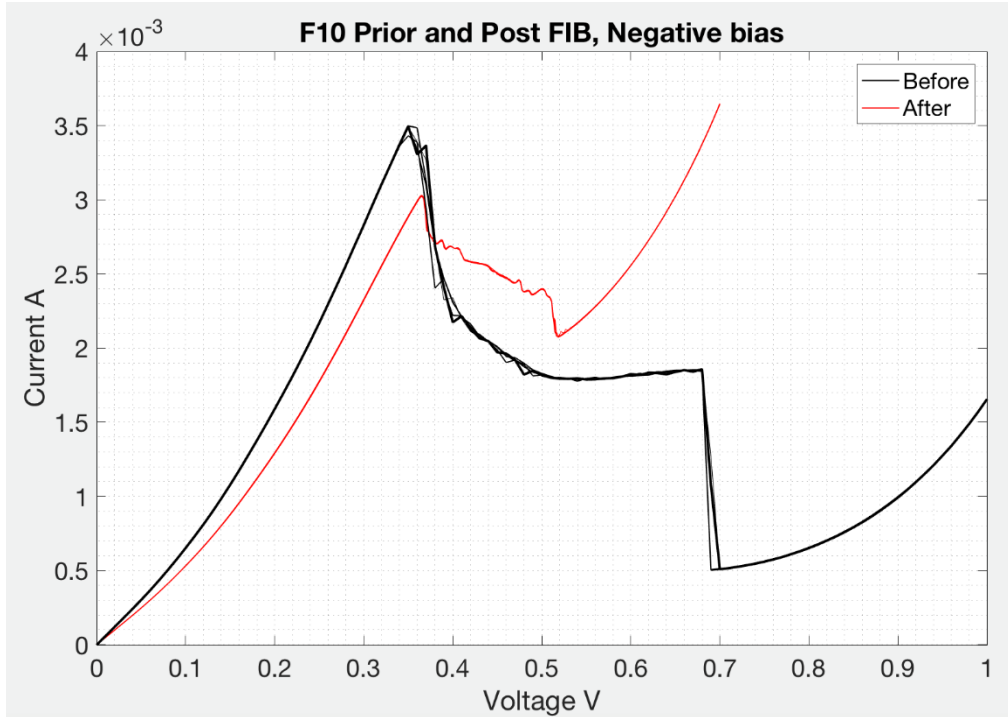


Figure 4.15: IV characteristic of device F10 with prominent bumps in NDR (of voltage range of 0.36V ~ 0.51V) grouped near the resonance peak and the valley. We note high in parallel resistance and minimal in series resistance.

4.2.9 Dot etch

We attempted again at creating the smallest active region, for this we milled a dot like structure. Our success rate was only 17% with only two functioning devices post FIB. Including the active bridge the average surface area of our devices was 4.92 μm^2 (Table 4.8).

Device	Area i μm^2	initial resonance peak	initial resonance valley	PVRi	final resonance peak	final resonance valley	PVRf	Area f μm^2	Area reduction
D4	25	(0.37V, 7.30mA)	(0.75V, 0.92mA)	7.93	(0.59V, 3.10mA)	(0.6V, 1.24mA)	2.50	n/a	
F4	25	(0.36V, 7.3m0A)	(0.74V, 0.90mA)	8.11	(0.40V, 1.80mA)	(0.53V, 1.30mA)	1.38	3.81	6.56

Table 4.8: Devices etched with the dot design, showing their initial and final (post FIB) peak and valley positions; and their corresponding peak to valley ratio (PVR).

Close observation of the SEM images of devices D4,I4,J4 (Fig 4.16) show that we milled in such a way that no current would be able to flow from the top contact to the bottom contact. We observe the repeated mistake in figure 4.7 based on the arrow etch.

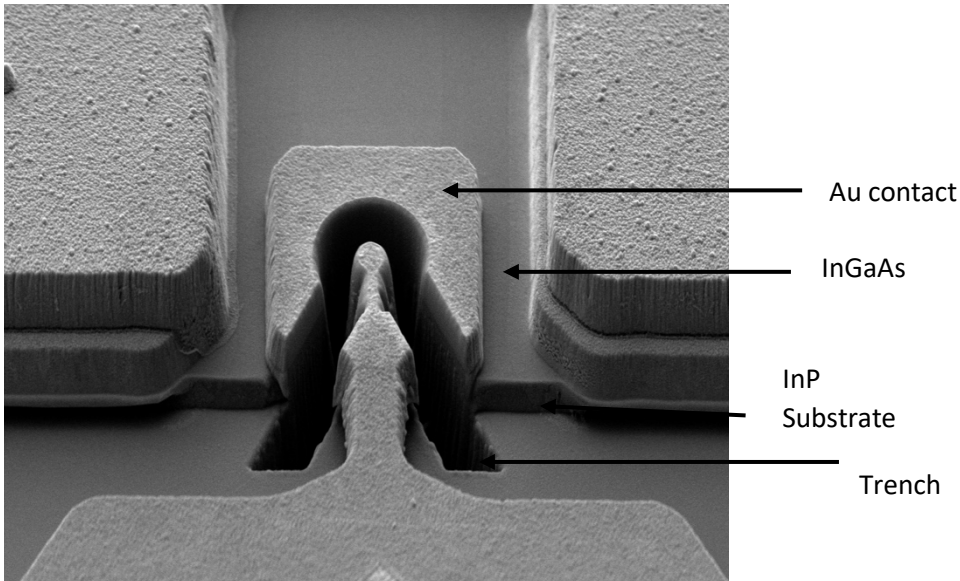


Figure 4.16: SEM image of a dot etch design showing the trenches within the InGaAs that isolated the active region thus, causing an open circuit. The intended active area includes the dot and the irregular shape above the air bridge.

Although we noted two working devices (D4,F4) we report that F4 was the only device functioning appropriately with an NDR region that suggested slight bumps. Whereas device D4 exhibited highly unstable characteristics (Fig 4.17). We were only able to observe one sweep that suggested the slightest hint of a peak and valley and two in low resistance states whereas the other three exhibited highly unstable, high resistance states.

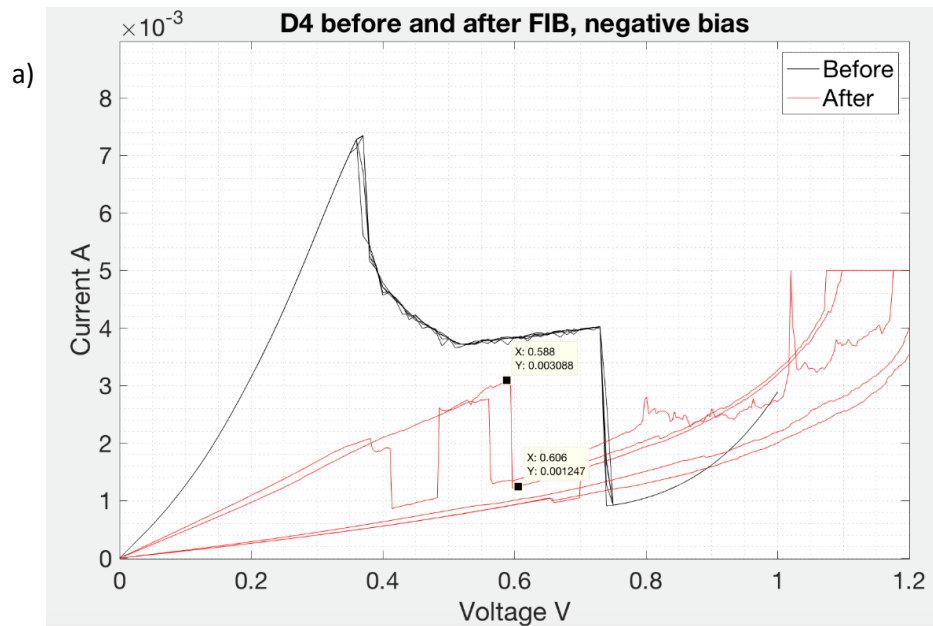


Figure 4.17: a) IV characterises of device D4 showing highly unstable regions and single peak and valley points.

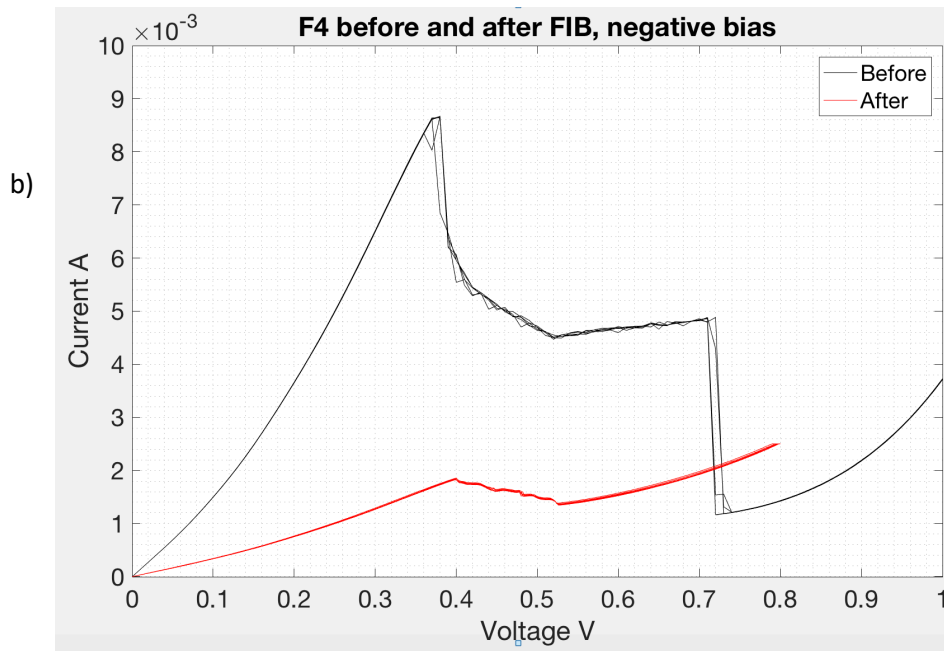


Figure 4.17: b) IV characteristics of device F4 displaying a small PVR, both etched with the dot design.

4.3 Analysis

Exploring a wide variety of etch designs yielded two main results (in addition to the many defective devices); namely slight bumps in the NDR region and a secondary resonance peak. Overall, we observe four devices that exhibited both features. The four devices that showed stable and repeatable bumps were F10, G10, G1 (square etches respectively) and B4 (lateral etch). We compare and contrast the resemblance of such features to that of the multiple resonant peaks due to 0D and 1D confinement reported in previous studies.

4.3.1 Defective devices

The most prominent artefact of such were devices that did not exhibit a clear NDR region and resembled that of a resistor. In particular such devices showed high in parallel resistance (Fig 4.8) which we attribute such due to defects induced by the FIB implantation. It has been reported that the effect of heat in double barrier quantum wells yield compositional disordering which in turn invoke the change of the super lattice to a different alloy altering its properties i.e. refractive index and band gap [3]. Other studies have reported on the effect of Ga ion implantation on the superlattice and comment on the interdiffusion of Ga in the superlattice turning the sample into a crystal of different properties [4]. To evaluate such defects we require TEM scans or photoluminescence measurements however what is evident with such device is an increase of in parallel resistance. Such has been attributed to the Ga ion converting n+ doped GaAs to highly resistive p-type [3].

4.3.2 Increased bit rate

In line with our initial objective which was to increase the bit density (per unit area) of these devices. We have observed that etching with the use of a FIB produces some functioning RTD with a clear NDR structure. Bagci's most optimum scheme for bit extraction outputted a maximum of 8 bits for every $4 \mu\text{m}^2$ (2 bits/ μm^2). We report 8 functioning devices with an increased bit density ranging from 2.2 bits/ μm^2 to 3.5 bits/ μm^2 (57% increase). Incorporating the extra features observed previously (bumps in the NDR) could potentially further increase the bit density of up to 8 bits/ μm^2 . This would significantly reduce the number of concatenated devices required, from 16 devices each with an area $4 \mu\text{m}^2$ to output a desired total of B=128 bits to 2 devices (measuring $4 \mu\text{m}^2$) outputting a total B=160 bits. However we first require elucidating such features and uncovering their origin.

4.3.3 Second resonance Peak

An emergent feature found in four devices (D11, B4, A11 B7) was a second resonance peak similar to that observed in Fig 4.5 & Fig 4.11. The smallest lateral dimension found on these devices after etching with the FIB are summarised in Table 4.9

Device	D11 (Diamond)	B4 (Ring + Triangle)	A11 (Diamond)	B7 (Lateral)
Lateral dimension (nm)	55.6	277	133	599

Table 4.9 Smallest lateral size (nm) found on the devices which exhibited a double resonant peak. The smallest lateral dimension found being 55.6 nm-device D11 (diamond etch).

The effects of increased confinement in [5],[6] became evident when the lateral dimensions of their devices measured to be of the order of 100 nm. The requirement reported in the literature [5] is that the physical structure needs to be adequately small such that the quantisation of the momenta (laterally) is $> kt$. To determine the possible energies of the confined states we need to evaluate the radial potential within the confined structure which would depend on the potential height Φ_T (dependent on Fermi level pinning), lateral size of the physical structure R and the depletion depth. The Discrete electron levels corresponding to the confined states is given by

$$\Delta E = \sqrt{\left(\frac{\Phi_T}{m^*}\right) \frac{\hbar}{R}} \quad (5)$$

m^* is the electron's effective mass in the well. R is the dimension of our confined region.

The feature categorised as 'small bumps' found in the NDR (Fig 4.18) bare similar resemblance to the features observed in [2]. They have on average an inter-voltage spacing of 2.5mV (Table 4.10) which would imply the states being split by 1.25 meV, however unlike [5] such are not equally split but increase incrementally. In comparison with the findings in [5] the authors observed a subband splitting of 20 meV. Considering the feature categorised as 'second resonant peak' our average inter-voltage separation (peak to peak) was 110 mV, implying an average subband splitting of the discrete states of

55 meV although closer to the subband splitting observed in previous studies we are only able to report on a single state as opposed to up to 8.

[4.3.4 Minute features superimposed in NDR](#)

The features uncovered in four devices with similar etch designs bare close resemblance to the features observed in [6] & [5] which were attributed to increased confinement due to lateral confinement of the heterostructure. G1, F10 and G10 were etched to the same design (square) and similar parameters, whereas B4 was etched laterally (Fig 4.23).

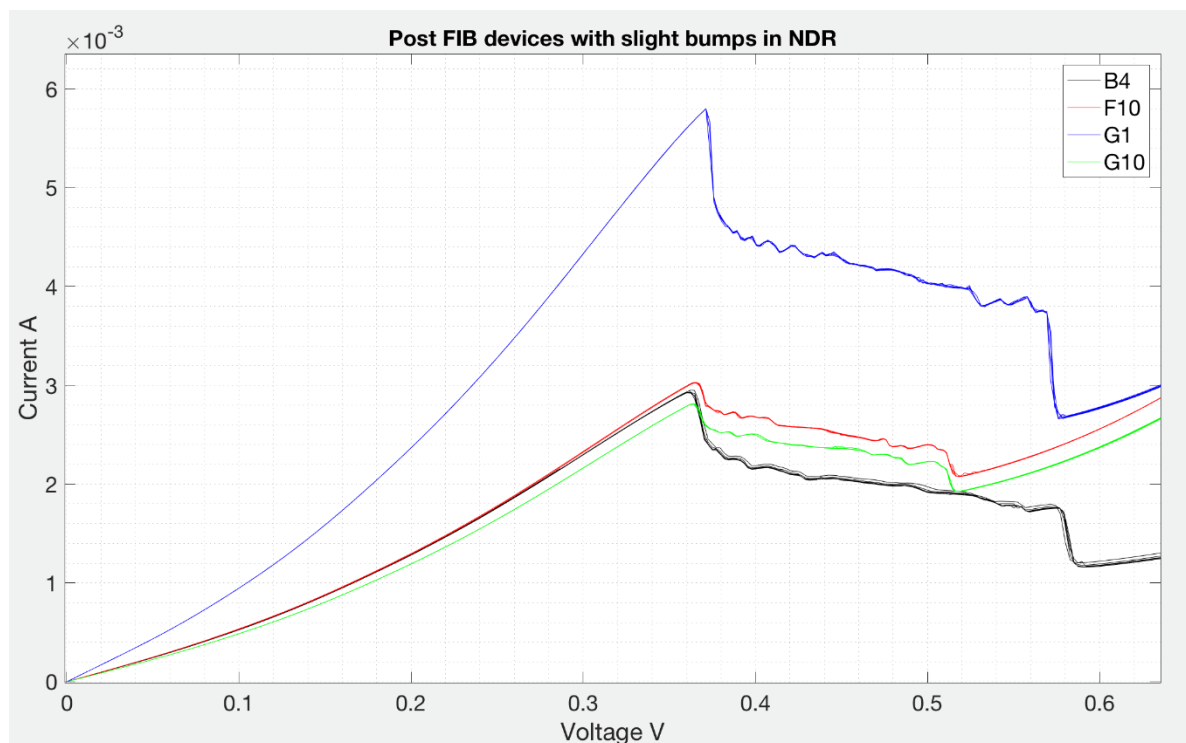


Figure 4.18: IV characteristics of four devices that showed bumps in the NDR, the bumps appear to be grouped in two regions, after the resonance peak and before the valley, such bumps appear in similar voltage ranges.

[4.3.5 G1 Square etch](#)

One of the most prominent of features post FIB was seen with G1 (Fig 4.19), this device featured a square cavity, with features prominent in the NDR that manifests its self as bumps. We observed a decrease in the PVR as a result and an increase in current density which we would expect as a result of in parallel resistance that may be induced by the Ga^+ beam.

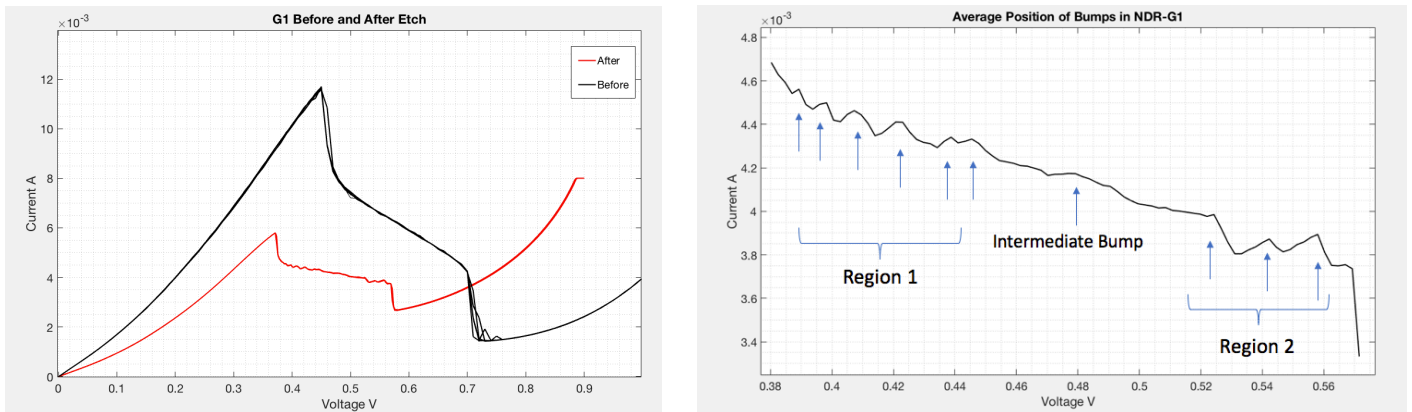


Figure 4.19: (left) IV characteristic of G1, before and after FIB treatment. (Right) Bumps within the NDR region, showing two clusters of bumps and an intermediate bump, 10 bumps in total.

The NDR region exhibits a more pronounced difference, while we observed a total of ten minute bumps and ridges in the NDR superimposed within the NDR. To rule out the possibility of noise, we averaged our results over five repeated measurements and observed the same features. We observed a grouping of the bumps after the resonance peak and before the resonance valley, additionally our averages hinted at an intermediate bump that lay between the two clustered regions.

4.3.6 F10 Square Etch

We observe similar features in a device with the same etch design. We observed groupings of the bumps and an intermediate feature (Fig 4.20).

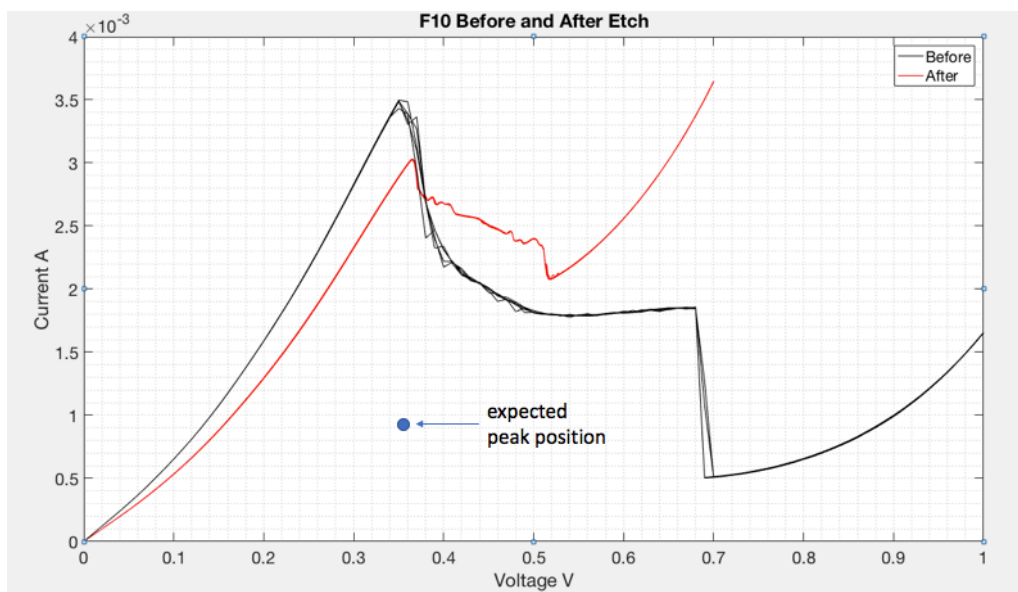


Figure 4.20: Large in parallel resistance causes a shift in the resonance current (red curve), small bumps can be observed within the NDR region of the post FIB IV characteristic.

However, we observed eight bumps superimposed in the NDR which was a decrease compared to the previous device, namely only four in region one and three in region two despite having more possible area of confinement (see Fig 4.23).

In addition to this, parallel resistance of approximately 65Ω was found in the post modified device, most likely induced by the FIB procedure. Such was evident as the resonance position was observed at a much higher current.

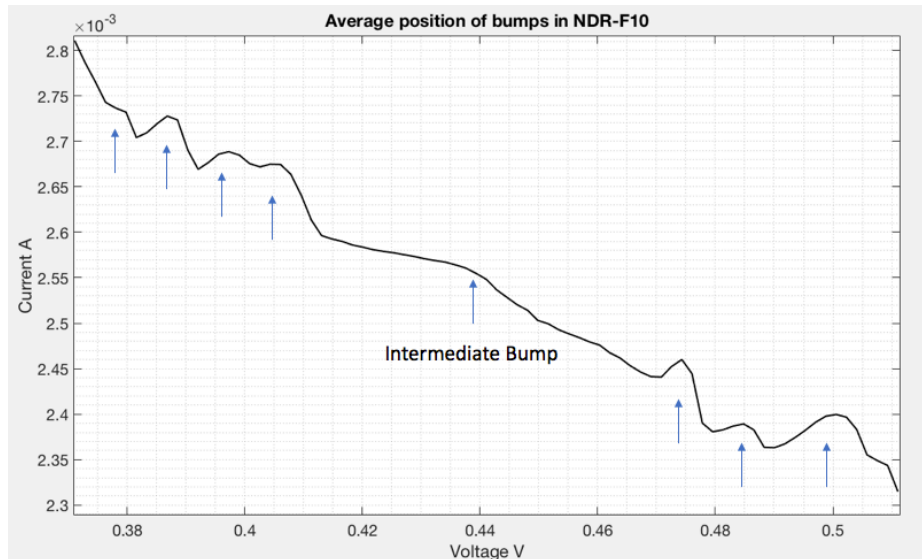


Figure 4.21: Eight bumps super imposed on NDR, with the presence of an intermediate bump.

4.3.7 B4 Lateral Etch

By reducing the lateral dimension of our RTD from $8 \times 8 \mu\text{m}$ to $4 \times 8 \mu\text{m}$, we observed the same pattern however with less broadening of the two regions, in total nine bumps and minimal in series and parallel resistance was observed.

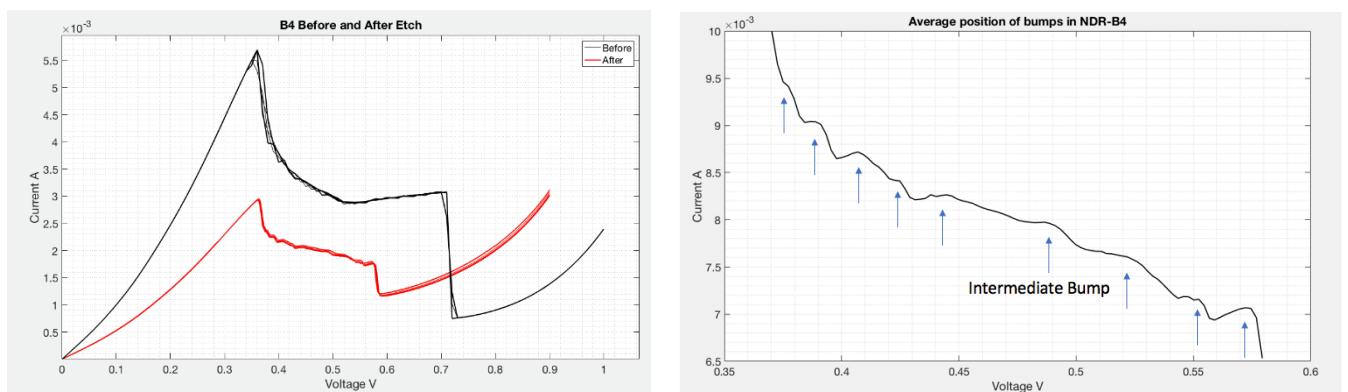


Figure 4.22: (left) IV characteristic of B4, before and after FIB treatment. (Right) Bumps within the NDR region, showing two clusters of bumps and an intermediate bump, 9 bumps in total.

Due to the nature of the etch designs of device G1, G10 and F10; it is difficult to narrow down the exact area of potential confinement however we observe areas within the corners of cavity that exhibit the smallest area. In particular the dimensions ranged from $0.14\ \mu\text{m} \sim 0.63\ \mu\text{m}$. In previous literature [5], the lateral dimension by which features within the NDR was observed occurred when $x \sim 0.15\ \mu\text{m}$. However, we observe such with device B4 (chip 1), which was not etched in such a way where areas of confinement would take place. Namely the smallest constricted lateral dimension induced by the FIB is $1.63\ \mu\text{m}$. At such scale one would not expect in theory confinement in 1 dimension.

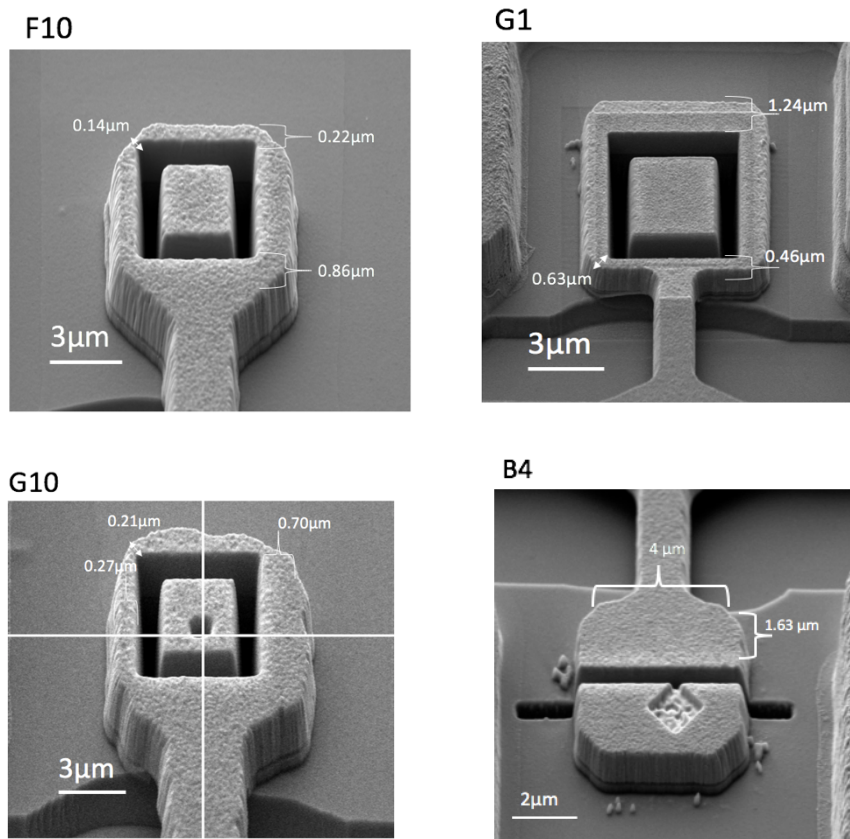


Figure 4.23: SEM images of etched devices that gave consistent bumps within NDR and showing the smallest regions that may have induced confinement effects in 1 & 0 dimensions.

Within region 2 of our NDR we observe a consistent number of bumps with an equal voltage spacing ($\pm 3\text{mV}$). However within region 1 the number of bumps fluctuate depending on the device, we observe an incremental broadening of 1mV within the inter bump distance increasing as the voltage increased with the square etched devices (Table 4.9). With B4 (laterally etched device) an average of 2mV broadening was observed within region 1 as voltage increased. If such features are due to confinement we would expect an equal inter voltage distance between the bumps.

G1	G10	F10	B4
38.7 mV	37.64 mV	37.98 mV	37.73 mV
39.82 mV	38.51 mV	38.86 mV	38.89 mV
40.73 mV	39.74 mV	39.73 mV	40.7 mV
42.08 mV	45.69 mV	40.61 mV	42.48 mV
43.87 mV	47.43 mV	43.76 mV	44.47 mV
44.55 mV	48.31 mV	47.43 mV	48.88 mV
47.93 mV	50.06 mV	48.48 mV	52.17 mV
52.42 mV		50.06 mV	54.79 mV
54.23 mV			57.49 mV
55.8 mV			

Table 4.10: Voltage position of bumps with region 1 (green) and region 2 (blue), showing the position of the intermediate bump (red).

4.3.8 Low temperature measurements of bumps

The IV characteristics of the RTDs suggest large amounts of instability within the device which may be attributed to deformations and defects induced by the FIB. IV characteristics show a wide range of effects post FIB such as slight bumps in the NDR region to, the suggestion of a new resonance peak characterised by a second PDR. At cryogenic temperatures we hoped to observe a set of features that would later assist in deducing the possible causes of the aforementioned effects. Our preliminary LT (low temperature) measurements were conducted in the LT probe station for ease as such an apparatus did not require prebonded devices. The helium flow cryostat was used once we bonded our samples using the micro wire bonder. Our preliminary measurements took significantly longer, in addition to this the micro positioner of the probes were less sensitive to adjustments; coupled with the sharpness of the probes the contacts of our device were significantly scratched and damaged where the probes came into contact. Another limitation of the low temperature probe station was that the source of cooling, liquid nitrogen limited our cooling to only 77k.

We aimed at uncovering any hidden extra peaks/bumps due to increased confinement due to the FIB. We drew our attention to only a handful of devices and etch designs as our preliminary probe station measurements ruled out the successful and redundant that are no longer functioning devices post FIB. In these measurements we observed multiple differences in the IV characteristics. We uncovered changes in the tunnelling region, resonance peak, NDR region, valley position and thermionic emission region/second PDR. Such features are present in both positive and negative sweeps of the IV characteristic, however in many cases such details are most prominent in the negative sweeps only.

In particular we observed two main differences; an increased resonance peak current and decreased resonance peak current. An increase in resonant tunnelling current at lower temperature is not characteristic of the tunnelling process. The authors of [7] attribute this to an increase in substrate mobility. A decrease in peak current at lower temperatures however has been attributed to scatter induced broadening of the resonance levels [8]. At higher temperatures, the increase in current is due to an increase of thermally active transport means such as thermionic emission. In many cases we observed a decrease in stability which we may attribute to the probe-contact surface due to the unpredictable nature of the LT micro positioners and probes. We observe the effects of LT conditions of an unmodified $3 \times 3 \mu\text{m}$ device mesa G11 (Fig 4.24). Overall we observe an increase in resistance at LT, up to a voltage of 0.12v we observed an exponential like increase in the tunnelling region of the LT device and the resonance peak position had shifted relative to the RT peak by (+0.03V,-0.04mA) and a valley shift of (+0.10V,-2.36mA), a smaller PVR is also evident, such has been commented on previously in literature and has been attributed to the fact that the valley current increases faster with temperature than the peak current [9].

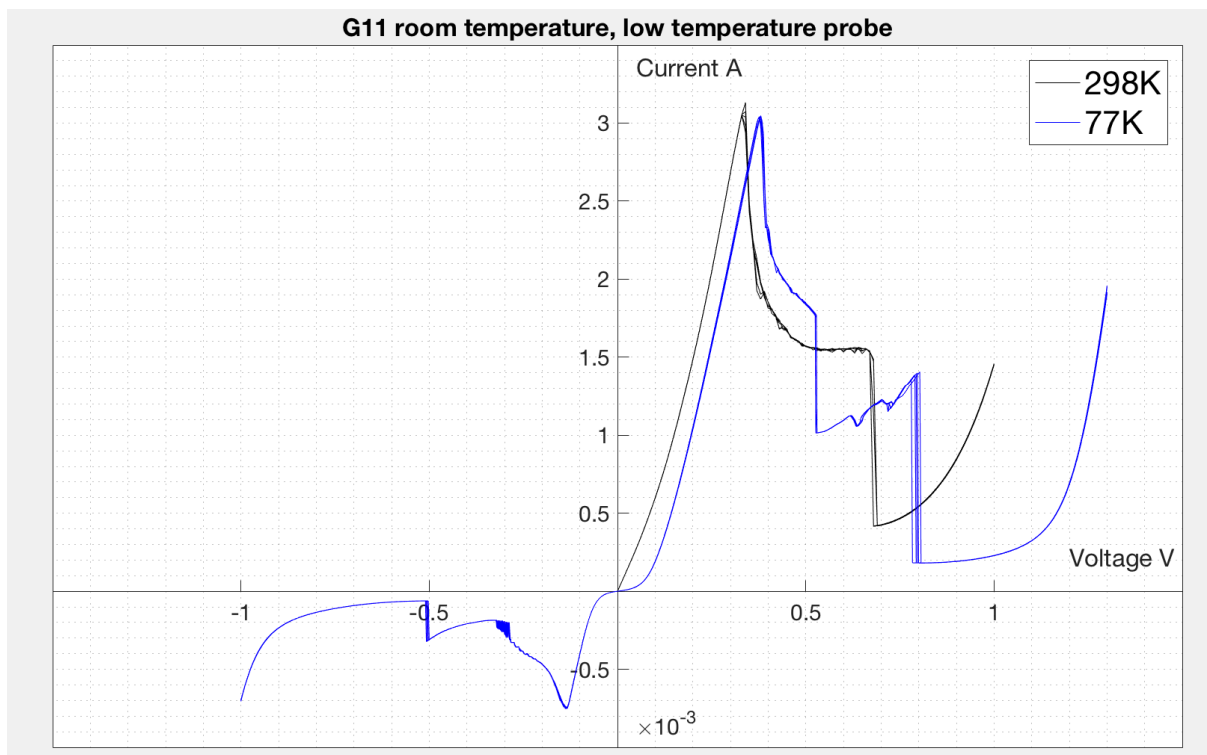


Figure 4.24: IV characteristic of G11 at room temperature and low temperature showing a slight shift in peak and valley position.

To minimise errors induced by the probe tips, we resorted to the helium flow cryostat. We bonded our devices with the method outlined in sec 3.4. The low success rate deemed many of our samples defective in particular the devices which exhibited a secondary resonance peak were all damaged by the ball bonding process and we were unable to test such at low temperature. However we observe an emergence of fine structure in the form of bumps within the NDR under the positive bias. The bumps previously observed under the negative bias remains as we lower temperature, this was the case of device G1 (Fig 4.25).

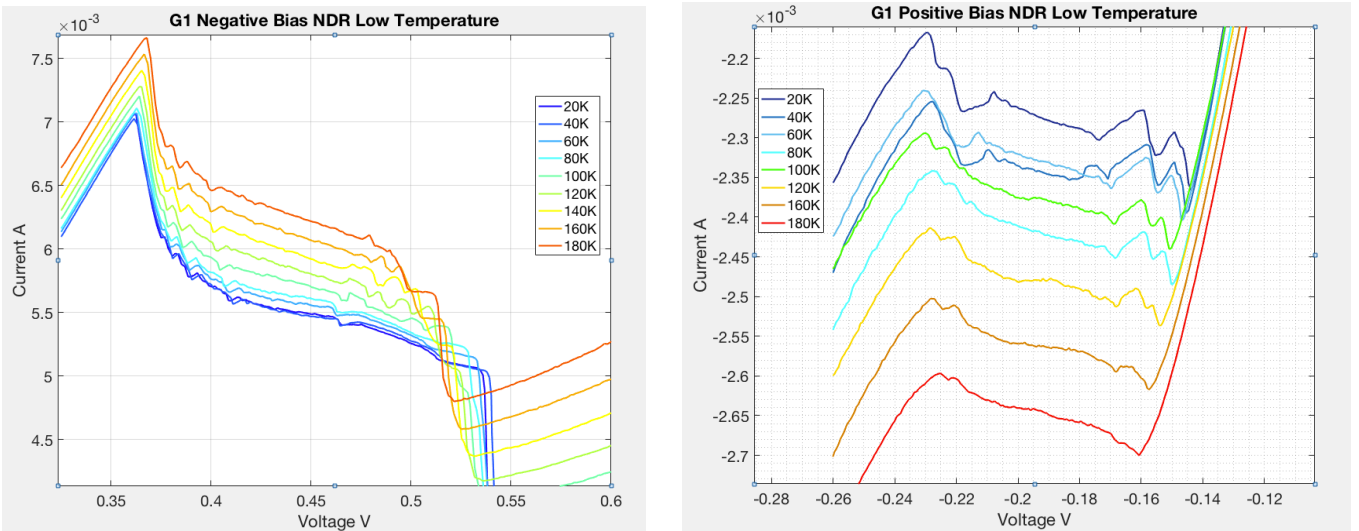


Figure 4.25: Variation of NDR with temperature, showing the prominence of bumps as temperature is lowered, in particular in the positive bias where at room temperature such bumps were non-existent.

We initially speculate that the emergence of such bumps are due to confinement in the 1 and 0 dimensional case, however as we have observed such with B4 which was not etched in such a way that would cause lateral confinement. We observe the shift in voltage of the resonance peak and compare such to the shift in the bumps and notice that at lower temperatures the resonance peak shifts to lower voltages whereas the contrary applies to the bumps. In particular, the bumps appear to follow to be coupled to the valley voltage (Fig 4.26).

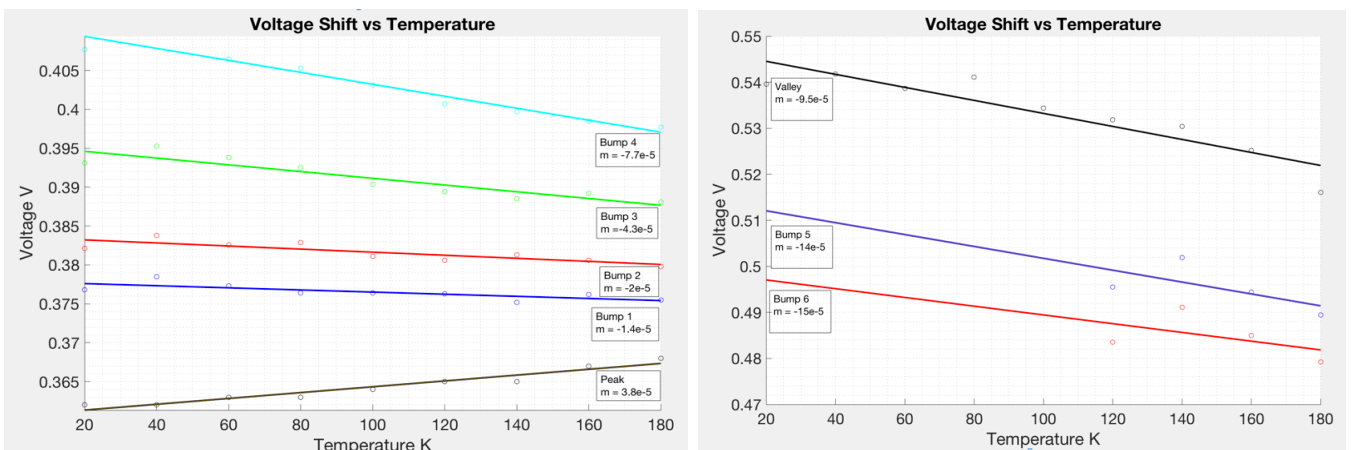


Figure 4.26: Voltage shift as a function of temperature for the resonance peak and the first four bumps (left) and the final three (right). We observe the positive gradient of the resonance peak, and the negative gradient of the bumps and valley.

We also observe a more pronounced temperature dependence of the resistance of the bumps that bare greater resemblance to the valley resistance than the peak resistance. We observe a minute dependence of the peak on temperature, such is evident under both bias.

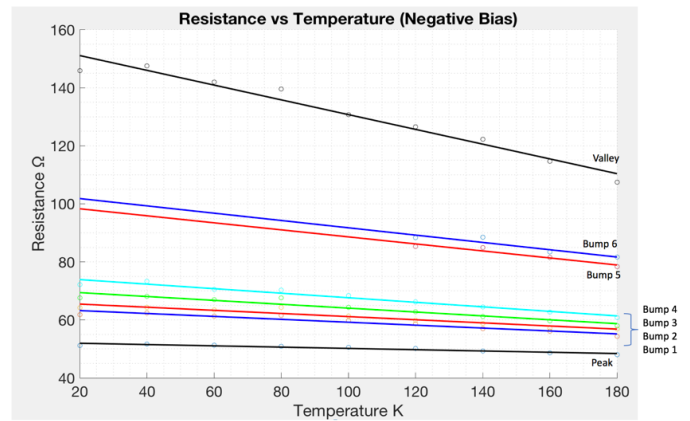
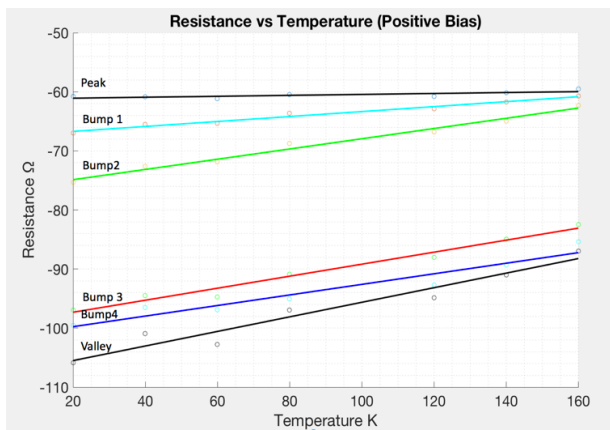


Figure 4.27: Resistance vs temperature of peak, bumps and valley. Peaks appear to have a more pronounced temperature dependence similar to that of the valley.

The shifting of the resonance peak to slightly lower voltages at lower temperatures which may be due to a drop of contact in series resistance of the InGaAs, the decrease in current is expected due as the excess leakage current being reduced.

4.4 Discussion and conclusion

We have etched a number of RTDs with different designs in an attempt to create multiple areas of confinement by laterally reducing the dimensions of the active regions. Our designs ranged from simple geometries such as small holes or diamonds to more complex shapes such as rings and triangles. We conclude that the square etch design was most successful in producing repeated results that resembled 1D or OD confinement. The square etch followed a relatively simple geometry and at the same time attempted at maximising the likelihood of confined regions by incorporating corners small enough to accommodate quantum confinement. We encountered a number of issues with FIB-sample alignment that rendered many devices defective. The intensity of the Ga⁺ beam has been shown to induce in parallel resistance and alter the doping profile of the heterostructures. We have shown that it is possible to produce fully functioning RTDs that operate on a smaller scale with a lower operating power and show clear signs of resonant tunnelling with visible NDR regions and with a PVR as high as 1.5.

We observed devices that exhibited a secondary resonance peak with an average intervoltage separation of 110 mV, implying an average subband splitting of the discrete states of 55 meV, however further theoretical analysis is required to elucidate the origin of such feature.

We also observed another set of repeated features with four devices, three of which were of the same etch type (square cavity). We initially interpreted said results as increased confinement as we observed the signature multi bump characteristic on the IV spectrum in the NDR region, we rule out the possibility of the FIB causing these changes as the FIB parameters were kept unchanged. These results bare similar resemblance to the work referenced in Sec 2.9 and hence speculate the emergence of quantum confinement in higher order states (0, 1 dimension). However, the fact that such features are found in device B4 which was etched in such a way where no lateral confinement would take occur

would suggested that such features may not be characteristic of resonant tunnelling. The average voltage separation of such were 2.5mV which wold imply the states being split by 1.25 meV. These values are significantly smaller than the values observed in [5]. We conduct low temperature IV characteristics of our devices and observe that such bumps, behave similarly to the valley which may suggest that the origin of these features may depend on Fowler-Nordheim tunneling as opposed to resonant tunnelling.

Bibliography

- [1] J. Roberts, "Using Quantum Confinement to Uniquely Identify Devices," *Scientific Reports*, vol. 5, no. 16456, 2015.
- [2] S. Tarucha, "Resonant tunneling through one- and zero-dimensional states constricted by AlGaAs/GaAs/AlGaAs heterojunctions and high-resistance regions induced by focused Ga ion-beam implantation," *Physical Review B*, vol. 41, no. 8, 1990.
- [3] Y. E. a. Y. Suzuki, "Defects in Ga Ion Implanted GaAs-AlAs MQW Structures," *Japanese Journal of Applied Physics*, vol. 25, no. 11, 1986.
- [4] Y. Y. Hirayama, "Compositional Disorder of the GaAs-AlGaAs Superlattice by Ga Focused Ion Beam Implantation and its Application to Submicrom Structure Fabrication," *Japanese Journal of Applied Physics*, 1985.
- [5] S. T. e. al., "Resonant tunneling through one- and zero-dimensional states constricted by AlGaAs/GaAs/AlGaAs heterojunctions and high-resistance regions induced by focused Ga ion-beam implantation," *Physical Review B*, vol. 41, no. 8, 1990.
- [6] J. M. Reed, "Observation of Discrete Electronic States in a Zero Dimensional Semiconductor Nanostructure," *Physical Review Letters*, vol. 60, no. 6, 1987.
- [7] R. M. Iutzi, "Defect and Temperature Dependence of Tunneling in InAs/GaSb Heterojunctions," *In Press*.
- [8] C. J. G. Y. C. H. a. W. R. A. Chen J, "The I-V characteristics of double-barrier resonant tunneling diodes: observation and calculation on their temperature dependence and asymmetry," *J. Appl. Phys.*, vol. 70, no. 31, pp. 31-36, 1991.
- [9] J. S. D Li, "Temperature -Dependence of Negative Differential Resistance in GaN/AlGaN Resonant Tunneling Structures," *IOP Publishing*, vol. 28, 2013.
- [10] U. I. B. e. al., "Generating Secrets From Quantum Confinement Physically Unclonable Functions," *In Press*, 2016.
- [11] U. I. B. e. al., "Generating Secrets From Quantum Confinement Physically Unclonable Functions," *In Press*, 2016.
- [12] h.-L. T. e. al., "Resonant tunneling through a double GaAs/AlAs superlattice barrier, single quantum well heterostructure," *Applied Physics Letters*, vol. 49, no. 156, 1986.
- [13] J. e. a. M. M. e. al., "Extremely Uniform Tunnel Barriers for Low-Cost Device Manufacture," *IEEE ELECTRON DEVICE LETTERS*, vol. 36, no. 6, 2015.
- [14] D. H. C. e. al., "Physics-Based RTD Current-Voltage Equations," *IEEE Electron Device Letters*, vol. 17, no. 5, 1996.

Chapter 5- Conclusions and Further Work

5.1 Conclusions

In this work we have attempted at increasing the bit density issue of the InGaAs/AlAs resonant tunnelling diodes QCPUF by laterally constricting our active area to induce multiple areas of confinement. Currently such PUFs rely on the resonance peak position to extract 6~8 bits per device through a digitisation method proposed by Bagci. It has been observed that resonant tunnelling in zero dimensional nanostructures gives rise to fine structure within the NDR [1] of the IV characteristic of the RTD.

A number of issues were encountered in the preparation and processing of our samples. FIB-SEM alignment was an issue that produced devices that were inaccurately modified and reduced the number of functioning devices post FIB with a smaller bit density. Such inaccuracy at times isolated the conducting path of the RTD rendering such device as defective.

In addition to this the microwire bonder rendered many devices untestable, in many cases the diameter of our ball left little room for error when applying our initial bond, it was not uncommon for a SC to be caused due to the ball contacting both terminals. This was the most common cause for defective devices. Although such samples were still testable with a standard probe station it inhibited four terminal measurements to take place. Although resorting to the probe station provided ease and convenience, aggravation from probe contacts reduced the reliability and repeatability of our IV characteristics.

Out of 194 devices, 65 of which were etched, we applied a total of 8 variations of etches and observed approximately 28 devices were functioning post FIB and exhibited an a distinctive NDR. We report that the smallest surface area of a functioning device is $2.25 \mu\text{m}^2$, with a PVR of 4. Whereas previously the smallest surface area of such RTDs were $4 \mu\text{m}^2$, our modified device operated at 25% less power and have ultimately increased the bit density by a factor of 4.2.

Overall, we observed a number of interesting features such as instabilities, absence of an NDR region and features superimposed in NDR. In the majority of our post modified devices we observed some kind of in parallel resistance (and minimal in series resistance) which we attribute to the Ga ion beam converting n-type doping to highly resistive p-type doping [2]. Of particular prominence were two features; a secondary resonance peak and bumps within the NDR. Four devices exhibited a secondary resonance peak and we comment on the difficulty on verifying this result as such has not been previously seen before or attributed to tunnelling via 0D & 1D states. We speculate the emergence of two RTDs in series as a result of the FIB isolating specific regions of the RTD. An argument however that cannot be applied to device B7 which was etched laterally and showed the same characteristic secondary resonance peak, further work will aim towards elaborating such hypothesis. We initially conclude that the square etch was our most effective etch design, our aim was to introduce a simple geometry that at the same time maximised the likelihood of confined regions by incorporating corners with minimal dimensions. This etch design produced the recurring result of bumps superimposed within the NDR.

However a number of works have attributed bumps within the NDR due to increased dimensionality of confinement [3] [4] [1]. We initially speculate the origin of such bumps due to this effect and we observe that these features are grouped in two different regions, after the resonance peak and before the valley. An intermediate bump is typically seen in the range of 0.4-0.5V for all devices. These features are not equally split and we observed an incremental increase of such states within region one. Bumps within the NDR that have been attributed to confinement in the 0 & 1 dimensional tunnelling are equally split however in our case we observe an irregular spacing split across the three regions.

Low temperature measurements were carried out to observe the effect of temperature on the small bumps, such was carried out within the helium flow cryostat. We report on a linear relationship on the voltage shift of the bumps, peak and valley vs temperature. Interestingly the bumps within the NDR behave similarly to the valley voltage position in that they scale negatively unlike the resonance peak position which scales positively with temperature. Such may suggest that these minute features are a result of some thermionic effect such as Fowler-Nordheim tunnelling rather than resonant tunnelling. However if such features are dependent on uncontrollable parameters in the fabrication and sample preparation stage, incorporating the bumps as minutia would potentially increase the bit density to 8 bits/ μm^2). This would significantly reduce the number of concatenated devices required, from 16 devices each with an area $4 \mu\text{m}^2$ to output a desired total of B=128 bits to 2 devices (measuring $4 \mu\text{m}^2$) outputting a total B=160 bits.

[5.2 Further work](#)

By repeating more lateral measurements where the lateral dimension of the active region is reduced to approximately 50-100nm would be a first step in realising increased confinement due to 1D & 0D states as seen in [4]. To verify our results we would require etching more RTD with the FIB, paying particular attention to the diamond and square etch as these produced the most interesting results. Prior to this, more care in SEM-FIB alignment will ensure that we have accurate etched dimensions. To elucidate the effect of the Ga ion beam on the InGaAs/AlAs interface, controlling the beam intensity and etch rate may reduce the number of defective/unstable devices.

Many devices post FIB may be preserved had an alternative channel due to an error in ball bonding not formed. Although directly controlling the diameter of the gold ball is infeasible we are able to limit the size by reducing the amount of gold wire exposed to the plasma. In future preparation of our samples it is recommended that the initial bond will not be to the sample contact but rather to the pad (Fig 3.6), this is because the wedge bond formed after the initial ball and wire has formed, is significantly smaller in surface area and due to the nature of wedge bonding, will be less likely in removing parts of the sample contact during lift off.

A full theoretical analysis is required to gain understanding on the origin of the minute bumps found within the NDR. Further knowledge of the potential profile within the laterally confined regions due to Fermi level pinning [1] will help us rule out effects due to quantum confinement. For this we require modelling the band structure, evaluating the depletion region by understanding how such variation of the depletion profile with the change of carrier density behaves. Additionally, considering the effect of subband mixing at the interface and such effect on the IV characteristic as suggested by Bryant [5]. Modelling the electron concentration and conduction band profiles of our resonant tunnelling structure by solving continuity and Poisson equations will evaluate the position of such features [3] as well as plotting subband energies as a function of the lateral potential [4].

On the other hand we speculate that the emergence of a secondary resonance peak may be due to a secondary RTD being in series as an effect of the FIB. As we characterised such by an intermediate NDR between the two peaks, the addition of a resistor in series with the device and observing the effect on the NDR and the peaks may suggest if such is due to resonant tunnelling or other effects.

Bibliography

- [1] e. a. M.Reed, "Observation of Discrete Electronic States in a Zero Dimensional Semiconductor Nanostructure," *PRL*, vol. 60, no. 6, 1988.
- [2] Y. H. e. a. Y. Suzuki, "Defects in Ga+ Ion Implanted GaAs–AlAs MQW Structures," *Japanese Journal of Applied Physics.*, vol. 25, no. 11, 1986.
- [3] R. e. a. M. Van Hove, "Zero-dimensional states in submicron double-barrier heterostructures laterally constricted by hydrogen plasma isolation," *Journal of applied physics*, vol. 72, no. 158, 1991.
- [4] e. a. S.Tarucha, "Resonant tunneling through one- and zero-dimensional states constricted by AlGaAs–As/GaAs/AlGaAs–As heterojunctions and high-resistance regions induced by focused Ga ion-beam implantation," *Physical review B*, vol. 41, no. 8, 1990.
- [5] G.Bryant, "Resonant tunnelling in zero-dimensional nanostructures," *Physical Review B*, vol. 39, no. 5, 1988.